Mineralium Deposita
https://doi.org/10.1007/s00126-024-01324-w

ARTICLE

El Zorro: early Jurassic intrusion-related gold (IRG) mineralization in the oldest, western-most segment of the Andean Cordillera of Northern Chile

Eduardo Fritis[1] · Nicholas H. S. Oliver[2,4] · Michael C. Rowe[1] · Julie V. Rowland[1] · Zeffron C. Reeves[3] · Huiqing Huang[4]

Received: 9 February 2024 / Accepted: 1 October 2024

Abstract

The El Zorro gold district is the most recent gold discovery in the Coastal Cordillera of northern Chile. Ternera is the largest deposit in the district with total resources currently estimated at 1.282 Moz. New geology, geochemistry and geochronology data indicate that hydrothermal mineralization is mostly hosted within felsic to intermediate, ilmenite-bearing calc-alkaline dikes and stocks of the Upper Triassic to Lower Jurassic Relincho Pluton, and some of the adjacent Devonian to Carboniferous metasediments of the Chañaral Epimetamorphic Complex. Sheeted veins, veinlets, and fault zones with quartz, low amounts of pyrite, pyrrhotite and arsenopyrite, and local calcite are surrounded by narrow haloes of albite-biotite-quartz ± sulfides-K-feldspar-sericite-chlorite. Gold (mostly in the veins) is associated with elevated W-Bi and also As-Te-Sn, and not with iron enrichment or base metals, even though this system is proximal (~ 20 km) to IOCG and IOA deposits of the Coastal Cordillera. The main phase of gold mineralization occurred soon after emplacement of tonalitic dikes and granodiorite from the Relincho and Cuevitas plutons (U–Pb zircon between ~ 205 and 190 Ma), about 80 m.y. later than the development of orogenic fabrics. An absolute upper age limit is provided by compositionally distinct ore-cutting mafic dikes dated at 175–170 Ma (U–Pb apatite). The deposit falls into the intrusion-related gold category, as indicated by the cutting of earlier orogenic fabrics, the metal and alteration associations, and the spatial and temporal connection to reduced ilmenite-series intrusions, which are also very similar geochemically to the 'type-locality' IRG intrusions of the Tintina Belt in Yukon/Alaska. The El Zorro gold district represents the oldest and geologically western-most mineralizing event in the Central Andes of northern Chile, consistent with its time–space placement within the tectonic framework of easterly-younging mineralization and igneous activity in the Chilean Cordillera.

Keywords U–Pb geochronology · Whole-rock geochemistry · El Zorro gold district · Coastal Cordillera · Intrusion-related gold · Northern Chile

Introduction

Based on the Andean (Cordilleran) Orogen, Sillitoe (1972) recognized relationships between metalliferous provinces and subduction zones—since then, this has been one the most popular topics of global study in economic geology (e.g., Oyarzún 2000; Maksaev et al. 2007; Richards et al. 2017). The south-central segment of the Andes of northern Chile is known globally for its copper endowment (e.g., Camus and Dilles 2001) but also contains significant gold (Cabello 2021) (Fig. 1). From west to east, mineralization decreases in age, and changes in style and metal associations, across four main morphotectonic units: the Coastal Cordillera, the Central Depression, the Precordillera and the Main Andes

Editorial handling: F. Tornos

✉ Eduardo Fritis
eduardo.fritis.perez@gmail.com

[1] School of Environment, The University of Auckland, Private Bag 92019, Auckland 1142, New Zealand

[2] HCOVGlobal Consultants, 6 Hancock Rd, Alligator Creek, Queensland 4816, Australia

[3] Tesoro Gold Limited, Level 48, 152-158, St Georges Terrace, Perth, WA, Australia

[4] Economic Geology Research Unit, Division of Tropical Environments and Societies, James Cook University, Townsville, Queensland 4811, Australia

Published online: 06 November 2024

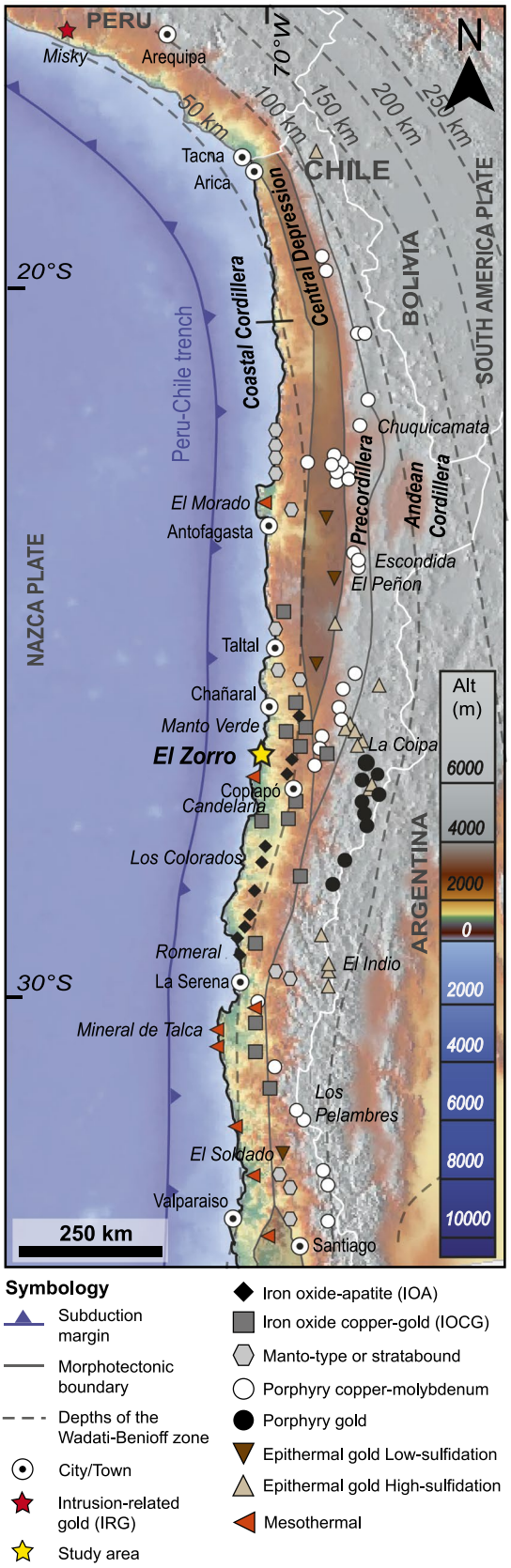

Fig. 1 Morphotectonic map of northern-central Chile showing the distribution of metallic ore deposits. Deposit locations were compiled from Palacios et al. (2014), Firth et al. (2015), Kojima et al. (2017), Tornos et al. (2021), Cabello (2021) and Maureira et al. (2022). Geotectonic domain boundaries were taken from SERNAGEOMIN (2003). The dashed lines give the depth in km to the Wadati-Benioff zone were taken from Cahill (1990)

Cordillera (SERNAGEOMIN 2003; Maksaev et al. 2007) (Fig. 2). This time–space evolution has long been considered to relate to changes in the position of maximum heat, magma and metal transfer due to the evolving geometry of the subducting Pacific Plate relative to the growth and evolution of the Andean margin (Hervé et al. 2007; García et al. 2017). Other controlling features on variations of mineralization type and style have included the age of the sub-continental lithosphere, the subduction mode, magma compositions, and the development and evolution of major transcurrent, transcrustal faults, such as the Atacama fault system (Bierlein et al. 2009; Richards et al. 2017; Seymour et al. 2020).

The westernmost unit of the northern Chile, the Coastal Cordillera (ca. 21° to 35°S) has a pre-Andean metasedimentary basement of Precambrian to Paleozoic age (Lucassen and Franz 1996; Oliveros et al. 2006; Charrier et al. 2007). Its western edge, along the coast, contains the oldest magmatic arc remnants, emplaced during the onset of the Andean orogeny from the end of the Upper Triassic into the Early Jurassic (Jara et al. 2021a, b) (Fig. 3).

Elsewhere within the Coastal Cordillera, most investigations have focused on understanding the genesis and evolution of iron and copper (± gold) deposits, mostly Cretaceous to Miocene in age. These include porphyry Cu-Au deposits (Reyes 1991; Maksaev et al. 2006; Escolme et al. 2020), stratabound 'Manto-type' Cu(-Ag), iron oxide-Cu-Au sensu stricto (IOCG) and iron oxide-apatite (IOA) (e.g., Sillitoe 2003; Chen et al. 2013; Richards and Mumin 2013; Richards et al. 2017; Barra et al. 2017; Tornos et al. 2021; del Real et al. 2023).

In 2017, Tesoro Gold Limited (https://tesorogold.com.au/) identified a significant gold-dominant resource, Ternera, in the El Zorro gold district, in the western-most part of the Coastal Cordillera, with resources estimated at 33.7 Mt at 1.18 g/t Au, totalling approximately 1.282 Moz of gold. Ternera and the satellite prospects are strongly spatially associated with intrusions previously determined to be latest Triassic to Jurassic in age. Given the Au-dominant mineralization, this raises the question of the style of mineralization, as it does not appear to be similar to previously described deposits in the Coastal Cordillera, with the possible exception of some prospects and minor deposits previously called lode-style, mesothermal- and/or orogenic gold (e.g., Vivallo et al. 2008; Firth et al. 2015; Kojima et al. 2017; Cabello

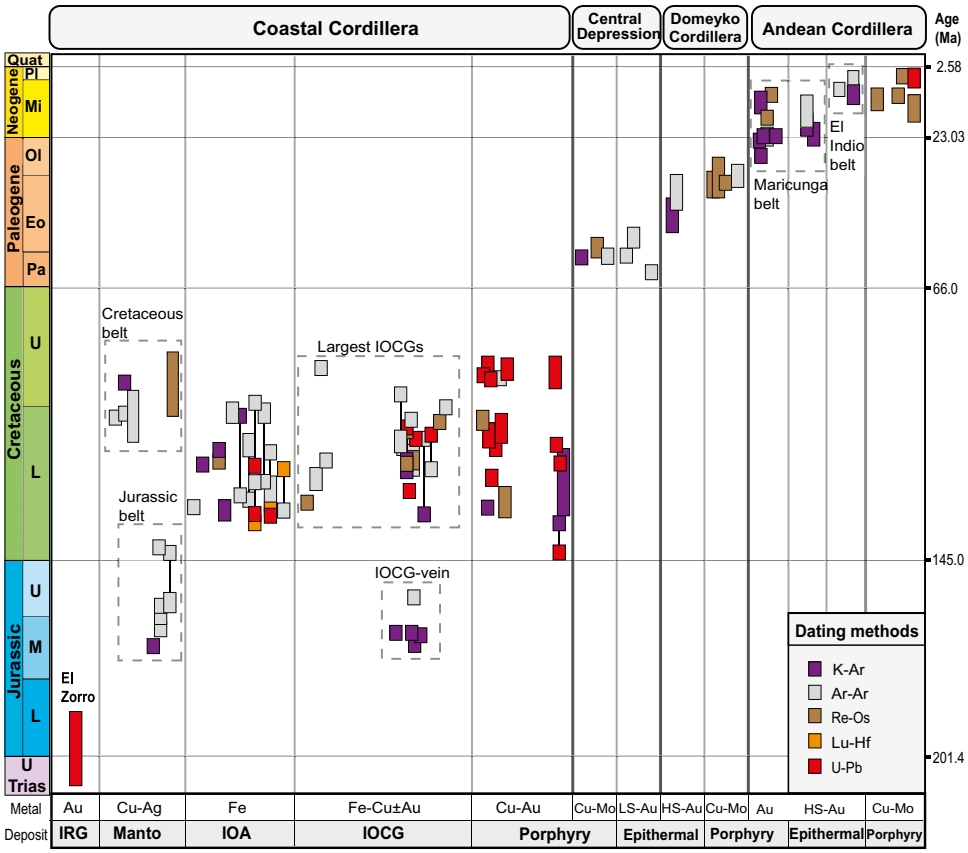

Fig. 2 Geochronological compilation of crystallization ages of different ore deposits, and some of their associated igneous crystallization ages throughout the Andean Cordillera (see ESM 1 Table A1). The age for IRGs is based on the age of crystallization of the igneous rocks that host the El Zorro gold district, and the results of this research (see Table 1). Deposit abbreviations: IRG – Intrusion related-gold; IOCG – Iron oxide copper–gold; IOA – Iron oxide-apatite; LS – Low Sulfidation; HS – High Sulfidation. Chronostratigraphic abbreviations: Eo – Eocene; L – Lower; M – Middle; Mi – Miocene; Ol – Oligocene; Pa – Paleocene; Pl – Pliocene; Quat – Quaternary; Trias – Triassic; U – Upper

2021). Its longitudinal position is also very interesting, lying west of all the other major Cu-Au deposits, in and around apparently pre-Cretaceous intrusions (Figs. 2 and 3). Since Hart and Goldfarb (2005) distinguished between orogenic and intrusion-related gold systems, the classification and understanding of gold-dominant or gold-only hydrothermal deposits has been debated (Aliyari et al. 2012; Cepedal et al. 2013; Firth et al. 2015; Yu et al. 2020, 2022). Despite many similarities (Yu et al. 2020 and references therein), IRGs are differentiated from orogenic gold deposits because in the former, ore and alteration assemblages are zoned around causative intrusions due to thermal disequilibrium with the wall rocks (Lang and Baker 2001; Hart and Goldfarb 2005; Groves et al. 2019). Likewise, there are similarities and differences between oxidized intrusive rocks with porphyry Cu-Au-Mo potential, and those more reduced intrusive hosting gold-only systems (e.g., Takagi and Tsukimura 1997; Orlandea and Vlad 2020).

Our preliminary field, petrographic, and geochemical work raises the possibility of affinities with deposits from the Tintina Belt, Alaska-Yukon, the 'type-locality' of IRG deposits (e.g., Lang and Baker 2001; Hart and Goldfarb 2005). This is based at least in part on recognition that the gold is spatially associated with reduced intrusions that appear to discordantly cut the orogenic fabrics at all scales (see below). The aim of this paper is to determine the nature of the mineralization style, the spatial and genetic relationship of the mineralization to the abundant intrusive rocks and also to the surrounding regionally metamorphosed sediments, and to develop a geochronologic understanding of these relationships, in the context of the regional evolution of the Coastal Cordillera.

Geology of the study area

We present here the results from the first detailed mapping, geochemistry and geochronology for the El Zorro gold district, with a focus on establishing the geological, geochemical and geochronological relationships between mineralization and the tectono-thermal evolution of the district.

There have been few studies conducted on the El Zorro gold district prior to our work. There was a district scale analysis of the intrusive history and fault network (Grocott and Taylor 2002), regional geochronology to match some of this (e.g. Godoy and Lara 1999), and a single K–Ar (whole-rock) age determination for the main deposit, Ternera (formerly named Coquetas, Vivallo et al. 2008). Coeur d'Alene Mines Corporation conducted drilling and generated 173 m of exploration adits at Coquetas (now Ternera) between 1990 and 1993, but this covered only a portion of the current resource. Several reports were generated on the gold

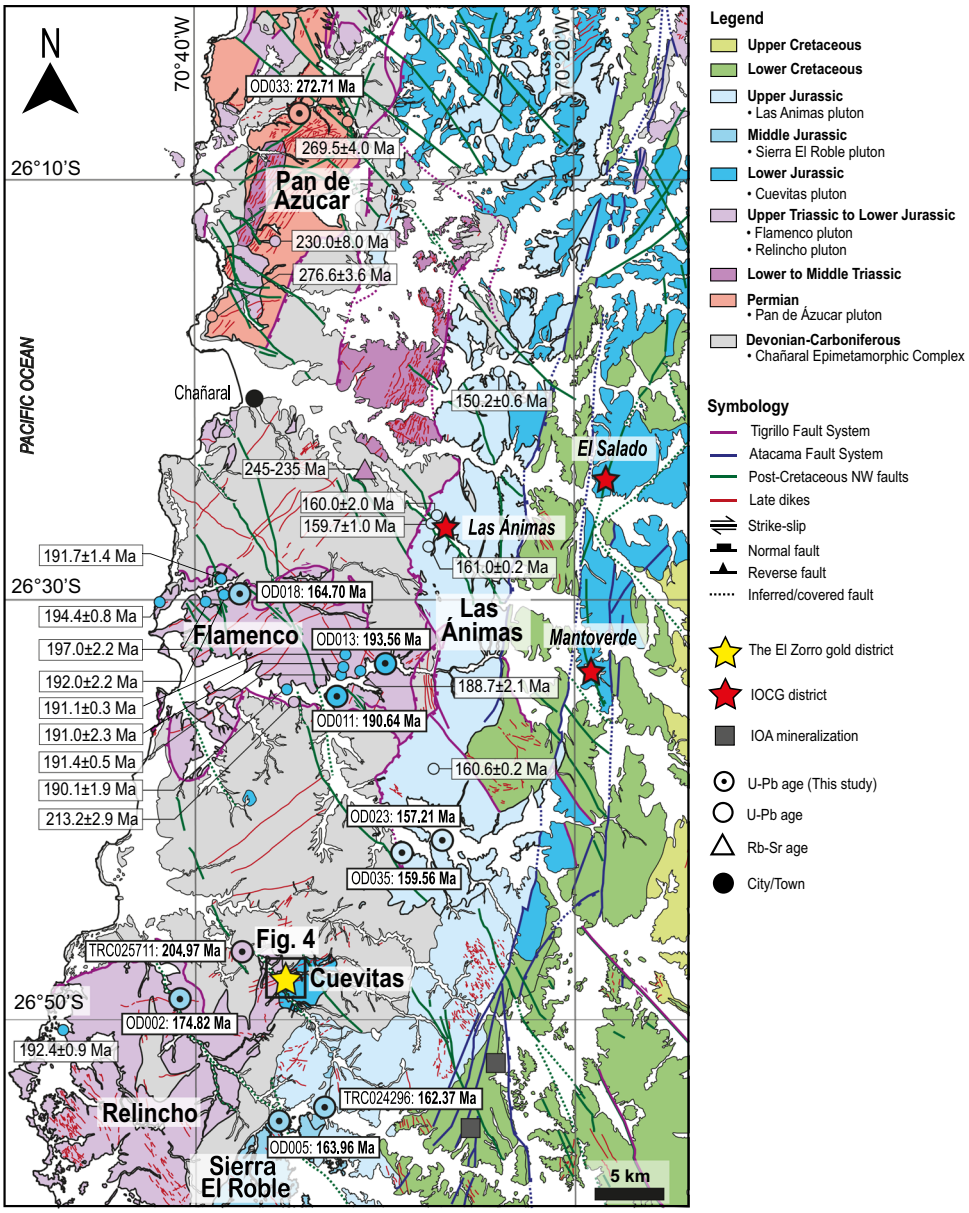

Fig. 3 Distribution of plutonic complexes, their emplacement ages, some major mineral deposits and major fault zones in the Coastal Cordillera between 26° to 27°S (modified after Godoy and Lara 1998, 1999; Lara and Godoy 1998; Grocott and Taylor 2002). Plutonic complexes analyzed in this study are highlighted in bold, and our results are shown with the larger circles. U–Pb geochronological data from the literature are shown with smaller symbols (ESM 1 Table A2)

grades, but with only limited geological information and a rudimentary map. They did not consider it economic with the prevailing gold price, and also ceased all their exploration activities in South America at this time. Our mapping and sampling commenced in detail in 2018 along with the initial Tesoro drilling.

Metasedimentary rocks

In the region (Fig. 3), the basement rocks of the Coastal Cordillera are assigned to the Chañaral Epimetamorphic Complex, a discontinuous, low-grade regional metamorphic belt comprising metaturbidites, metasediments and metabasalts of Devonian to earliest Permian age (Bahlburg and Hervé 1997; Godoy and Lara 1998, 1999; Godoy et al. 2003; Fuentes et al. 2018). These rocks are interpreted as a mélange at the frontal accretionary prism of the Late Paleozoic forearc, which developed during the first stage of the Gondwanan tectonic cycle (Charrier et al. 2007; Creixell et al. 2016; Oliveros et al. 2020).

These basement metasedimentary rocks around El Zorro and the broader region (Figs. 3 and 4) include monotonous sequences of Las Tórtolas Formation phyllites (with carbonaceous and volcaniclastic components) and quartzites of variable thickness, folded and regionally metamorphosed to greenschist facies. The likely sedimentation ages are more regionally constrained by detrital zircons in range 330 to 295 Ma (Bahlburg et al. 2009; Hervé et al. 2020). Regarding the regional metamorphism and ductile deformation that affected these rocks, Brook et al. (1986) have proposed

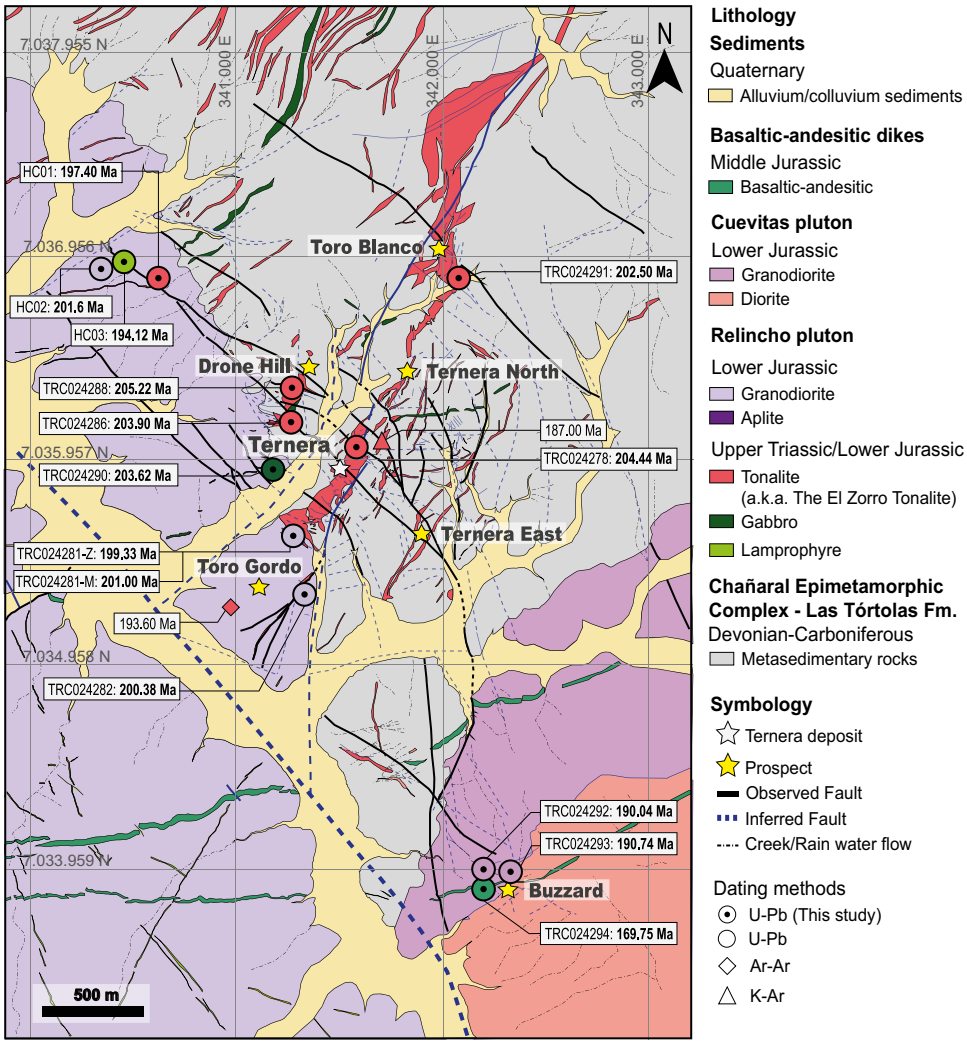

Fig. 4 Simplified geological map of the El Zorro gold district with the main prospects and key geochronological data

an age of 280 ± 15 Ma, based on Rb–Sr ages for low-grade metamorphism from the Las Tórtolas Formation. Berg and Baumann (1985) presented Rb–Sr whole rock ages of 245 to 235 Ma for regional metamorphism of quartzites and a phyllite from near Chañaral (Fig. 3); however, they noted incomplete isotopic homogenization and the likely effect of younger intrusive rocks, so the 245–235 Ma ages were considered a minimum. Both regionally and at El Zorro, there are younger intrusive, contact metamorphic and mineralization phases (see below).

Intrusive rocks

Magmatic arc plutonic complexes were emplaced into the Las Tórtolas Formation and other rocks of the Chañaral Epimetamorphic Complex (Fig. 3) from the Permian to the Early Cretaceous (Godoy and Lara 1998; 1999; SERNAGEOMIN 2003). Expressions of the Coastal Batholith in the district consist of Upper Triassic to Lower Jurassic plutonic rocks assigned to the Relincho and Cuevitas plutons (e.g., Godoy and Lara 1999; Jara et al. 2021a; this study, see below). A well-developed contact aureole of hornfels surrounds the intrusive bodies throughout the district where they interact with the Paleozoic basement (Godoy and Lara 1999; see below).

The El Zorro gold district is cut by several NW- to N-striking faults of variable displacement and uncertain kinematics. Grocott and Taylor (2002) inferred that these faults more regionally were predominantly post-Cretaceous. However, regionally, long-lived (initially pre-Cretaceous) NW and NE-striking faults (e.g., Tigrillo Fault System, Chañaral Shear Zone) cut basement and extend through cover sequences (Behn et al. 2001; Rodríguez et al. 2021; Reinoso et al. 2024), and are considered as controls on magma emplacement, and development of most of the Mesozoic mineral systems in northern Chile (Gow and Walshe 2005). At El Zorro, crosscutting relationships between faults and intrusions are complex: some faults cut some intrusions, but some intrusions cut some faults (see below).

Shapes and sizes vary from larger plutons through to smaller stocks, most commonly with monzogranodiorite, granodiorite and dioritic compositions, with abundant intermediate to mafic dikes. Notably, with the exception of the youngest basaltic dikes, these intrusions all predate the main Cretaceous intrusions that lie adjacent to the large IOCG district to the east and south (Fig. 3).

Sampling and analytical methods

Extensive field mapping was conducted in the area to better understand the nature of the mineralization style, and the temporal, spatial and genetic relationship of the mineralization to the abundant intrusive rocks and also to the surrounding regionally metamorphosed sediments. Twenty-four samples were selected for U–Pb in zircon, titanite, apatite or monazite geochronological analysis, fifteen for the local El Zorro gold district and nine for the broader region. Geochemical data were obtained by a variety of analytical techniques (fusion XRF, lithium borate fusion ICP-MS and four-acid ICP-MS); the results were compiled for ten corresponding geochronology samples in the local El Zorro gold district, along with thirty others from surface outcrops and district exploration drill holes (Fig. 4). A comprehensive geochemical database of fresh, altered and mineralized rocks from the Ternera drilling program is also presented (four-acid-digest ICP-MS), to constrain aspects of the alteration and metal associations and distributions. Analytical methods and representative results for geochemistry and U–Pb geochronology are presented in Table 1 and ESM 2, respectively. Full geochemistry and U–Pb analytical results are presented in ESM 1 Table A3 and A4, respectively. The large database of four-acid ICP-MS results for the Ternera orebody and surrounding areas is presented in ESM Table A5.

Results of geologic investigations

Primary features and cross-cutting relationships

The Relincho and Cuevitas plutons are the largest intrusions within the El Zorro gold district (Fig. 4). They intrude and cut the bedding and foliation within the Paleozoic units of the Chañaral Epimetamorphic Complex, with zones of hornfels reported around them (Godoy and Lara 1999; see below). We observed hornfels, locally containing cordierite and rare sillimanite porphyroblasts in aluminous rocks, and patchy cm- to dm-scale garnet-pyroxene-wollastonite skarns in uncommon calcareous layers, developed in zones up to 50 m wide (typically 1 to 10 m) around these plutons. Granodiorite of the Relincho Pluton exposed around the Toro Gordo prospect in the El Zorro area (Fig. 4) contains abundant primary plagioclase (~ 60 vol. %), hornblende, biotite, and quartz with accessory zircon and ilmenite. Primary magnetite is absent, and hematite is only observed as a weathering product. Granodiorite of the Cuevitas Pluton at Buzzard prospect (Fig. 4) is similar but with higher biotite/hornblende ratio, locally grades into K-feldspar-bearing granite (not mapped), and cuts into a large diorite (with lower quartz content) to the south. Contacts with the Relincho Pluton are largely obscured by Cenozoic alluvial sediments. Contacts with the main tonalite dikes that host mineralization are mutually cross-cutting (see below).

We define the El Zorro Tonalites (EZT) as part of the Relincho Pluton. They comprise a group of tabular hypabyssal dikes of variable thickness (0.3 to ~ 100 m) that host most of the gold mineralization in the district (Fig. 4). In fresh tonalite samples, primary minerals include phenocrysts (65–75%) of dominant plagioclase with lesser biotite, hornblende and minor quartz; and the groundmass comprise igneous-intergrown plagioclase and minor quartz crystals typically smaller than 0.3 mm. Accessory minerals include zircon, apatite and ilmenite (Fig. 5); primary magnetite is absent and hematite is only observed as a weathering product. Tonalite dikes also intrude the Paleozoic units of the Chañaral Epimetamorphic Complex, cutting regional metamorphic fabrics, and in places were injected along that foliation but with no internal ductile deformation features. Tonalites cut the granodiorite of the Relincho Pluton, and show local mingling relationships with the granodiorite (Fig. 4, 6 and 7). Lamprophyre and gabbroic dikes cut the tonalites (Fig. 6a).

Aplite dikes form small (dm- to 100 m scales in length, cm- to m-scale in width) dikes within the Relicho and Cuevitas granodiorites. In unaltered samples, quartz and perthitic plagioclase dominate their mineralogy, with accessory biotite, ilmenite and apatite. These aplites locally show a gradational transition into quartz-rich variants with local pyrite (see below).

At least three sets of mafic intrusions are observed (Fig. 4). The oldest, uncommon, gabbro dikes (m to -30 m wide, and rare small 100 m-scale stocks) intrude the Paleozoic units of the Chañaral Epimetamorphic Complex, cut the foliation within them, and cut some of the more felsic intrusions described below. Their primary mineralogy is dominated by euhedral to subhedral hornblende, plagioclase, and common biotite; rare orthopyroxene is overgrown by igneous hornblende. The main primary accessory minerals are apatite, titanite, ilmenite; rarely pyrrhotite and pyrite appear to be intergrown with igneous plagioclase. Apatites from these mafic dikes were successfully extracted for geochronology (see below).

Lamprophyre dikes are the second type of mafic intrusions (10 cm- to 5 m wide), typically much thinner in outcrop than most other dike types. Field recognition is difficult

Table 1 Whole-rock major, minor and trace elements geochemical data (major element oxides in wt. % and trace composition in ppm) for representative samples of the El Zorro gold district. Full data is provided in the ESM 1 Table A3. Mineral abbreviation from Whitney and Evans (2010)

Unit	Relincho pluton	Relincho pluton	Relincho pluton	Relincho pluton	Relincho pluton	Relincho pluton	Relincho pluton	Relincho pluton	Relincho pluton	Cuevitas pluton	Cuevitas pluton	Late dike	Late dike
Age	Upper Triassic/ Lower Jurassic	Upper Triassic/ Lower Jurassic	Upper Triassic/ Lower Jurassic	Upper Triassic/ Lower Jurassic	Upper Triassic/ Lower Jurassic	Upper Triassic/ Lower Jurassic	Upper Triassic/ Lower Jurassic	Upper Triassic/ Lower Jurassic	Upper Triassic/ Lower Jurassic	Lower Jurassic	Lower Jurassic	Middle Jurassic	Middle Jurassic
Sample	TRC024415	TRC024290	TRC024286	TRC024278	TRC025710	TRC025711	TRC024402	TRC024281	TRC024289	TRC024292	TRC024293	OD002	TRC024294
Rock type	Lamprophyre	Gabbro	Tonalite	Tonalite	Tonalite	Tonalite	Tonalite	Granodiorite	Aplite	Granodiorite/ granite	Granodiorite	Basaltic-andesitic	Basaltic-andesitic
Prospect	Ternera drillhole	Toro Gordo	Drone Hill	Ternera	–	–	Ternera drillhole	Toro Gordo	Drone Hill	Buzzard	Buzzard	Cutting Relincho Pluton	Buzzard
UTM East	341,895	341,389	341,453	341,782	337,777	337,777	341,757	341,504	341,521	342,411	342,523	332,325	342,402
UTM North	7,036,466	7,036,256	7,036,476	7,036,360	7,037,344	7,037,344	7,036,047	7,035,957	7,036,505	7,034,322	7,034,294	7,033,122	7,034,218
Alteration	Moderately strong	Weak	Weak to moderate	Weak to moderate	Weak	Weak to moderate	Strong	Weak to moderate	Weak	Weak to moderate	Weak to moderate	Weak	Weak
[a] *Major elements (%)* [ICP-AES]													
SiO_2	51.1	48.1	70.1	66.4	61.2	65.3	61.7	72.5	78.6	75	58.7	53.7	54.3
Al_2O_3	15.25	16.45	15.65	16.35	16.15	16.05	14.4	14.45	12.4	12.5	17.65	14.9	14.5
Fe_2O_3	6.84	9.21	3.03	3.94	5.92	4.18	4.74	2.08	0.72	3.24	7.71	10.8	10.5
CaO	8.2	9.61	2.97	4.31	6.1	3.84	4.38	1.81	1.34	1.21	6.8	6.86	7.52
MgO	4.65	9.05	1.13	2.51	4.21	1.83	1.53	0.66	0.22	1.02	3.42	2.84	5.07
Na_2O	4.16	1.9	4.69	4.45	3.92	4.38	4.24	3.83	5.31	2.8	3.43	3.71	3.19
K_2O	1.24	2.2	1.69	1.23	1.21	1.24	1.93	3.32	1.07	3.86	1.45	1.66	1.56
Cr_2O_3	0.002	0.043	0.002	0.009	0.02	0.002	0.003	< 0.002	0.002	0.005	< 0.002	0.006	0.013
TiO_2	1.19	1.03	0.38	0.51	0.73	0.57	0.48	0.2	0.1	0.38	0.82	2.34	1.85
MnO	0.11	0.2	0.06	0.07	0.09	0.07	0.04	0.04	0.01	0.05	0.14	0.17	0.17
P_2O_5	0.37	0.17	0.1	0.13	0.32	0.15	0.09	0.05	0.03	0.06	0.15	0.51	0.39
SrO	0.13	0.07	0.04	0.06	0.1	0.02	0.01	0.03	0.03	0.02	0.05	0.02	0.03
BaO	0.02	0.04	0.04	0.03	0.04	0.03	0.02	0.06	0.08	0.09	0.04	0.03	0.02
[b] LOI	5.31	2.96	0.9	1.67	1.98	3.12	5.19	1.18	0.89	1.48	0.91	1.39	0.81
Total	98.57	101.03	100.78	101.67	101.99	100.78	98.75	100.21	100.8	101.72	101.27	98.94	99.92
[c] *Trace elements (ppm)* [ICP–MS]													
Ba	184.5	309	314	213	371	234	171.5	460	663	772	298	260	195.5
Ce	64	28.1	33.3	30.9	65.1	28.2	16.8	52.4	57.7	50.5	32.7	68.1	52.4
Cr	10	320	10	60	140	10	20	10	10	40	10	40	100
Cs	7.51	5.24	1.67	2.41	3.15	3.33	1.87	1.2	0.48	2.19	2.94	2.01	6.7
Dy	4.59	3.71	2.43	2.63	3.73	2.81	2.56	1.58	1.5	3.3	3.97	9.98	8.63
Er	2.4	2.06	1.43	1.43	2.02	1.8	1.52	1.1	1	2.28	2.4	5.89	4.8
Eu	2.17	1.1	0.73	0.84	1.62	0.85	0.49	0.72	0.66	1	1.14	2.17	1.81
Ga	17.6	15.8	16.8	17.6	16.4	16.6	14.7	14.4	12.4	12.8	18.6	19.3	17.6
Gd	5.6	3.75	2.33	2.84	4.57	3.1	2.49	1.66	1.9	3.48	4.15	11.25	8.63
Hf	4.1	2.2	4.7	4.1	4.1	3.8	2.8	2.3	2.3	4.9	3.5	8.8	7.8
Ho	0.89	0.77	0.45	0.47	0.69	0.56	0.48	0.32	0.28	0.71	0.81	1.99	1.71
La	27.8	12.8	16.4	13.9	30.2	14.9	8	29.5	32.3	23.3	15.1	26.6	21.7
Lu	0.37	0.3	0.24	0.21	0.32	0.28	0.21	0.18	0.21	0.37	0.38	0.82	0.74

Table 1 (continued)

Unit	Relincho pluton	Relincho pluton	Relincho pluton	Relincho pluton	Relincho pluton	Relincho pluton	Relincho pluton	Relincho pluton	Relincho pluton	Cuevitas pluton	Cuevitas pluton	Late dike	Late dike
Nb	7.2	3.7	4.3	3.7	4.5	4.3	3.2	4.8	3	8.2	4.8	9.9	7.8
Nd	40.5	17.1	14.4	14.2	35.7	15.2	8.8	15.8	18.3	20	18.2	40.1	34
Pr	9.21	3.9	3.82	3.5	8.9	3.83	2.22	5.1	5.78	5.46	4.36	9.44	7.48
Rb	54.1	84.1	46.2	39.7	38.8	39.5	73	70.5	20.8	102.5	47.1	47.4	75.4
Sm	6.73	3.63	2.56	3.02	6.12	3.12	1.96	1.96	2.57	3.82	4.09	9.9	7.89
Sn	8	2	5	8	4	1	2	3	<1	3	2	4	4
Sr	1200	550	306	429	968	352	89	197	267	196	401	262	239
Ta	0.4	0.4	0.5	0.4	0.4	0.4	0.4	0.6	0.7	1.1	0.5	0.8	0.8
Tb	0.72	0.58	0.36	0.4	0.58	0.45	0.36	0.25	0.24	0.51	0.65	1.6	1.28
Th	3.21	2.2	4.88	3.16	7.39	3.47	3.03	8.99	15.8	18.9	3.86	10.45	9.8
Tm	0.35	0.32	0.23	0.21	0.3	0.27	0.22	0.15	0.18	0.34	0.35	0.84	0.71
U	0.53	0.41	1.06	0.81	1.22	0.82	0.81	0.91	0.94	2.12	0.81	2.51	2.11
V	189	272	43	81	133	73	67	27	<5	57	192	294	287
W	21	1	2	1	1	1	7	1	1	3	1	3	2
Y	22.8	18.8	13	13.4	19.2	16.3	13.9	9.5	9	20.2	21.8	53.7	46.9
Yb	2.05	1.88	1.41	1.44	1.97	1.74	1.49	1.08	1.19	2.45	2.28	5.22	4.57
Zr	160	74	190	146	168	150	105	73	62	167	125	357	286
[d] *Trace elements (ppm)* [ICP–MS]													
Ag	0.12	0.05	0.07	0.04	0.1	0.04	0.61	0.04	0.2	0.06	0.05	0.07	0.06
As	53.3	3.2	4.9	21.1	11.4	6.3	4730	3.4	1.6	3.4	1.7	5.6	4.3
Cd	0.05	0.08	0.08	0.05	0.12	0.1	<0.02	0.13	0.04	0.02	0.1	0.07	0.14
Co	32.2	32.1	5.1	10.1	19.9	8.7	11	2.7	1.5	3.3	17.7	23.4	28.2
Cu	58.6	8	19.6	9.4	108	10.4	60	4.2	3.4	27.3	27.1	137	116.5
Li	21.2	36.6	11.1	14.4	19.7	23	14.2	9.1	2	17.6	23.2	15.6	13.4
Mo	0.09	0.07	0.39	0.24	0.21	0.15	0.24	0.13	0.1	0.17	0.49	1.24	1.14
Ni	27.7	53.7	4.2	35.1	57.7	7.6	11.1	2.5	3.3	7.2	5.1	15.2	36.2
Pb	3.6	4.5	6.7	4.4	6	5	1.5	6.9	2.7	6.4	5.4	10.3	7.6
Sc	18.1	33.4	5.1	9.3	13	8.6	7.5	3	1.4	7.4	19.2	26.5	29.1
Tl	0.27	0.47	0.28	0.25	0.26	0.22	0.28	0.27	0.17	0.34	0.27	0.08	0.2
Zn	50	128	52	49	76	49	18	45	8	18	74	110	98

The analysis were conducted in ALS Labs, Lima, Peru, following the analytical procedures described in ALS (2022) for [a] ME–ICP06; [b] OA–GRA05; [c] ME–MS81; [d] ME–MS61

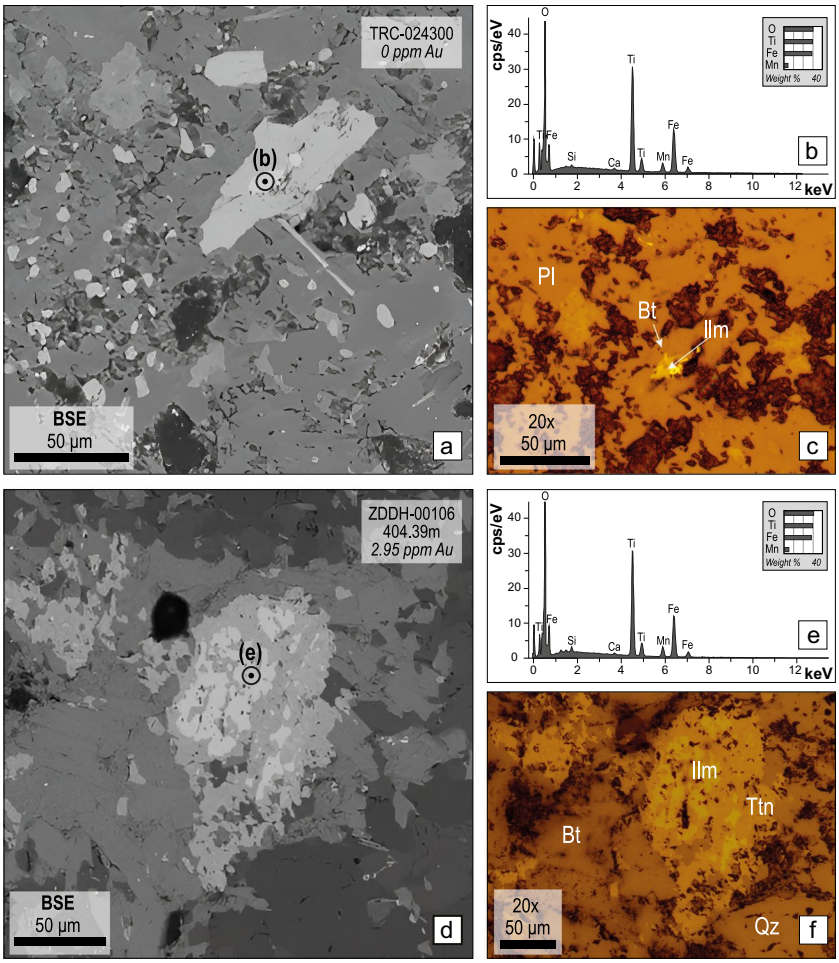

Fig. 5 Ilmenites in fresh (**a-c**) and altered (**d-f**) tonalites from El Zorro, demonstrating that they are part of the original igneous assemblage of the intrusions and that they also partially persist through the hydrothermal alteration process. (**a**, **d**) BSE images. (**b**, **e**) EDS analysis. (**c**, **f**) Polished section microphotographs, reflected light, plane polarized. (**a**, **c**) Show ilmenite included in igneous biotite, but there are multiple other small ilmenite and biotite grains on the left of the field of view; (**d**, **f**) show a large original grain of ilmenite partly replaced by titanite in a gold-mineralized sample

due to their fine grain size (~ 0.1 to 0.5 mm), but close inspection reveals abundant fine grained biotite (up to 60%). Relatively fresh examples commonly contain sprays of fine grained biotite as their only ferromagnesian silicate phase, intergrown with plagioclase, ilmenite and minor sulfides, but most lamprophyres are so strongly altered that their parent rock and sometimes primary mineralogy is obscured.

The youngest mafic intrusions in the El Zorro gold district are typically branching, m- to 30 m wide dikes of characteristically fresh basalt, basaltic andesite, andesite, and, in the core of thicker bodies, microgabbro and rare gabbro. Individual dikes may have > km strike length, most commonly on an E-W or ENE striking orientation. They cut across all other rock types, and notably cut across several faults, as well as mineralized veins. Although their field appearance is locally like some of the older mafic dikes, they are notable for their unaltered appearance, and the moderately common occurrence of olivine as a phenocryst phase, unlike all of the other mafic rocks in the district. They may be equigranular or moderately porphyritic, with phenocrysts of clinopyroxene, olivine and plagioclase set in a groundmass of plagioclase, hornblende and accessory biotite, ilmenite and apatite. Andesitic variants are olivine absent and have minor quartz.

Mineralization and alteration

The Ternera orebody is at an advanced exploration (prefeasibility) stage with over 60,000 m of diamond drilling for an estimated 33.7 Mt at 1.18 g/t Au, totalling approximately 1.282 Moz of gold as of September 2024. It is surrounded by several smaller (to date) prospects at km-scales (Fig. 4) as well as a series of early-stage exploration targets in the district defined by the western half of Fig. 3. Ternera is defined by a set of sheeted, individual and stockwork veins and several fault zones, is open at depth, and is predominantly hosted in tonalite of the Relincho Pluton, with < ~ 15% of the ore lying within adjacent metasedimentary rocks of the Las Tórtolas Formation, as well as minor granodiorite and diorite of the main Relincho Pluton, and several lamprophyre dikes.

Sheeted veins (0.5 to 20 mm wide) dominate the mineralization style (Fig. 7a, b), locally in spatial association with adjacent thicker individual or branching shear veins (Fig. 6a). Stockworks, breccias and mineralized fault zones also occur. Faults are dm- to m-scale in width, with m-to 100 m-scale (rarely bigger) offsets (Fig. 6a, b), with shredded veins, fault breccia, and brittle- to locally brittle-ductile

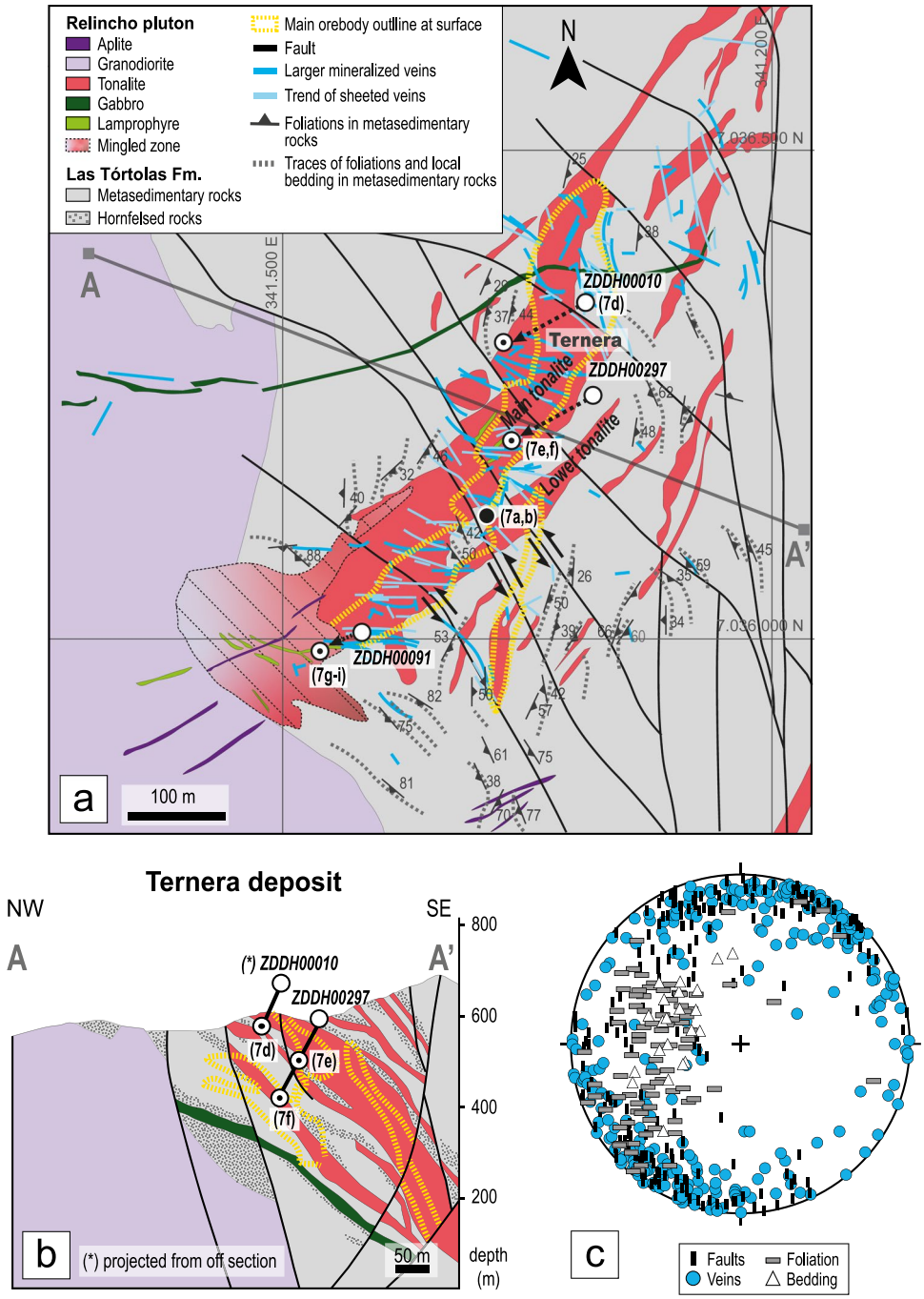

Fig. 6 (**a**) Geological map for the Ternera deposit and surrounding region, showing the primary features and cross-cutting relationships, and their relationship to key field features (Fig. 7 labels). The larger veins (darker blue) and trends of sheeted veins (paler blue) are mostly oblique to contacts and the wall rock foliation, and also have an apparent kinematic relationship to the low-displacement sinistral faults of which several are mineralized in the deposit vicinity. The orebody trace is based on results from surface channel samples and shallow drilling assays and is approximately 0.1 to 0.2 ppm. (**b**) Geological cross section of the Ternera deposit corresponding to A-A' on the map. The distribution of the hornfels shown (stippled pattern) is partly influenced by the drill spacing and the difficulty of clearly logging hornfelsed rocks in drill core and is a minimum estimate of its distribution. (**c**) Stereographic projection of poles to the main planar structures at Ternera, showing the predominance of steep, WNW striking veins and faults contrasting with broadly strike varying, moderately easterly dipping bedding and foliations in the Las Tórtolas Formation metasedimentary rocks. The position of the 7d, e and f figures shown on the drill traces have been projected from off-section to lie in the geologically equivalent position on this cross section, and do not represent the exact z-depth in the actual drill data

shear fabrics and a complex paragenesis; some faults with similar widths and offsets also appear to be barren, locally offset the orebody, and are dominated by clayey gouge. Although the orebody is roughly contained within tonalites, it is discordant to the boundaries in detail, and both sheeted and individual veins are arranged at a high angle to the tonalite margins (Fig. 6a, b). Some tonalite dikes were intruded along the foliation in the surrounding phyllites, but many cut across that foliation, and do not display any ductile deformation features that could be ascribed to the adjacent foliation (Fig. 7c). Statistically, the veins are WNW-striking and subvertical (Fig. 6c) whereas the bedding and foliation measurements are most commonly east-dipping with a wide strike variability and local tight to open folding of the bedding and refolding of the foliation. Veins in the metasedimentary rocks are sheeted, planar sided, unfolded, and characteristically cut the earlier foliation (Fig. 7d). In and around the orebody, veins, veinlets and fractures contain variable amounts of quartz, pyrite, biotite, calcite, actinolite, pyrrhotite and arsenopyrite, with rare occurrences of chalcopyrite

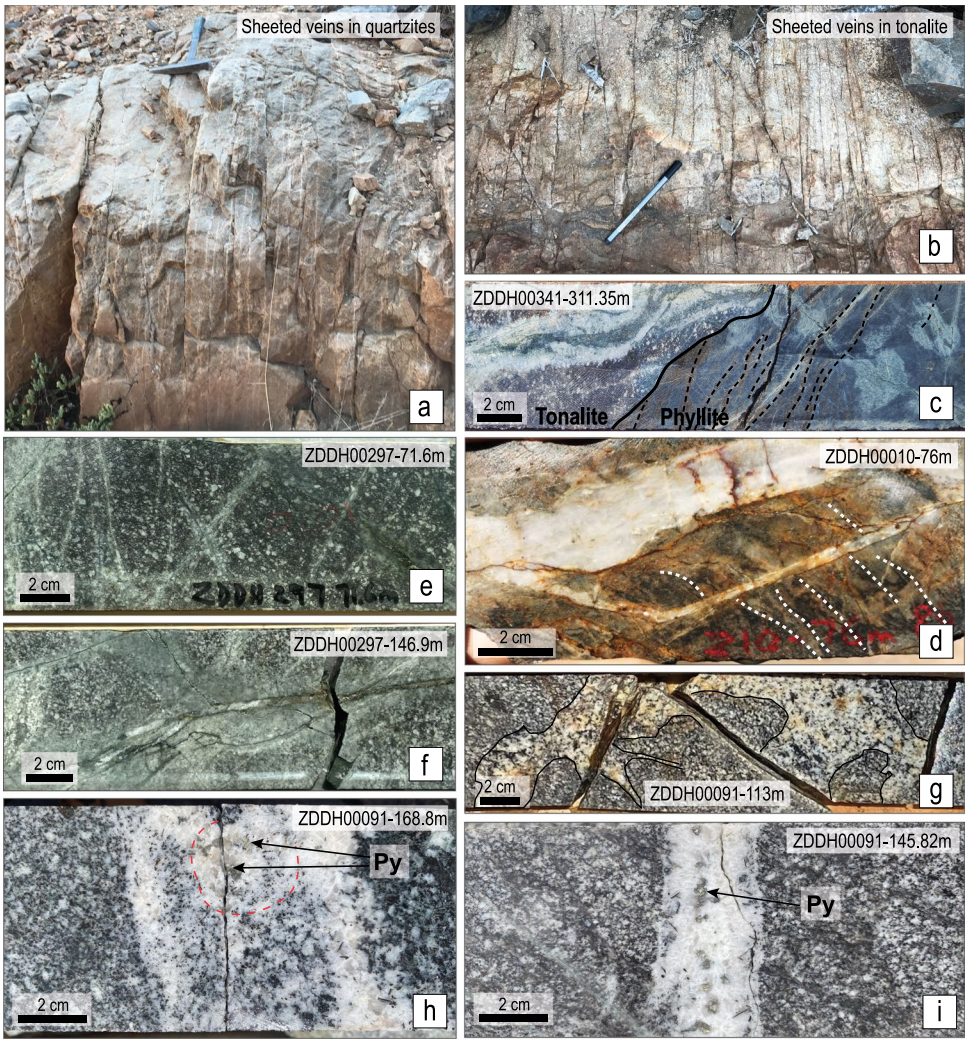

Fig. 7 Outcrops and core photographs of key relationships. (**a**) Typical steep-dipping sheeted quartz veins cut weakly mineralized metasedimentary rocks from Drone Hill prospect (see Fig. 4 for approximate position), but steep veins are also representative of those in phyllite adjacent to Ternera. (**b**) Typical steep-dipping sheeted quartz-sulfide veins cutting tonalites with partially preserved igneous texture from the main Ternera deposit. (**c**) Moderately mineralized sample showing tonalite dike cutting phyllites from Ternera East (Fig. 4). Solid line is the contact, dashed lines are traces of foliation and bedding within the phyllite. Note that veins and veinlets with surrounding pale to greyish alteration cut across the igneous fabric in the tonalite, but also extend into the phyllites where they cut discordantly across the foliation. (**d**) Drill core photograph of sheeted and branching quartz veins and related feldspar-sericite alteration with sulfides (rusty) cutting previous foliation (dashed white lines) in the Las Tortólas Formation phyllite. (**e**, **f**) Photographs from drill core showing progressive textural changes with tonalite ore hosts, from low Au grades (**e**) to high grade (**f**). Veins and veinlets are combinations of quartz, sulfides, calcite and actinolite; alteration is albite, biotite, calcite (earlier) and sericite-pyrite-chlorite (later). (**g**) Toro Gordo granodiorite (paler, outlined) mingled with Ternera tonalite, indicating co-emplacement along the contact zone shown in Fig. 6a. (**h**) An inferred miarolitic cavity (red dashed line) lies within late-magmatic aplite dikes cutting tonalite from the mingled zone shown in Fig. 6a. Pyrite occurs in the inner zone dominated by inferred hydrothermal quartz. (**i**) A zoned aplitic vein cutting the mingled zone tonalite-granodiorite. The vein shows euhedral biotite flakes on the edge intergrown with feldspar, then intergrown feldspar and quartz, and an innermost zone with quartz and pyrite inferred to represent a magmatic-hydrothermal transition

and/or sphalerite. Gold occurs primarily as free 1–25 µm grains within sulfides (mostly pyrrhotite, pyrite and arsenopyrite), along grain boundaries of quartz and sulfides, and within quartz or calcite. The rocks exhibit a wide range of alteration intensity (Fig. 5), broadly corresponding to gold endowment, but the alteration is most commonly spatially restricted around the veins at cm- to dm-scales, so that the orebody at broader than 5 m scales contains a mixture of fresh, altered and mineralized material (Fig. 7e, f). Altered samples show textural destruction and 'bleaching' (Fig. 7f), with a higher temperature association of albite, microcline, biotite, titanite, and quartz, with local zones of lower temperature alteration with combinations of actinolite, calcite, sericite, clinozoisite and chlorite, depending on the host

rock and the alteration intensity. Work is ongoing regarding details of the hydrothermal alteration, mineral chemistry and stable isotopes.

Lamprophyres are commonly found in or adjacent to mineralized faults and veins, and all of these locally cut across tonalite/metasedimentary rock contacts. They locally develop a weak foliation parallel to the adjacent structure (biotite and chlorite), which we infer reflects their emplacement into fault zones. They may contain good Au grades, locally in excess of 5 g/t (particularly at Ternera), as veins or veinlets with variable proportions of quartz, calcite, pyrite, pyrrhotite, arsenopyrite and biotite on vein edges, and alteration with disseminated pyrrhotite-pyrite set amongst albite, titanite, clinozoisite overprinting the plagioclase-biotite-dominant protolith.

The granodiorites are also cut by the mineralization, uncommonly as sheeted veins (southern end of Ternera; Fig. 6a) and more commonly in discrete, thicker sulfide-bearing quartz veins (dm- to m-scale), hosted in low-displacement faults and commonly with discontinuous lamprophyre lenses (Toro Gordo prospect, Fig. 4).

A zone of multiple intrusive phases is seen on the boundary between the main Relincho granodiorite and the tonalites hosting Ternera (Fig. 6a). Contacts between the intrusions are commonly irregular and lobate, and there are mutual cross-cutting relationships between different igneous phases, which we interpret as magmatic mingling (Fig. 7g) between the Relincho granodiorite and the tonalites. In drill core, from the same location, within microgranite or aplite dikes cutting the tonalites and granodiorite, we observed spherical growth of feldspar, quartz, biotite, and pyrite, with quartz growing into a cavity dominating the inner core, which we interpret as miarolitic cavities (Fig. 7h). Nearby, 2- 10-cm wide dikes of aplite show growth zoning from edges of intergrown biotite, sodic plagioclase and quartz to an inner zone of quartz and pyrite (Fig. 7i), and these thin dikes are cut by at least some low temperature sheeted veinlets of quartz and calcite with weak sericite-chlorite alteration haloes.

U–Pb geochronological results

Regional intrusions (26°07′S to 26°55′S)

The igneous domain defining the El Zorro gold district is defined in part by the presence of both older and younger intrusive rocks on its flanks. We determined a concordia age of 272.71 ± 2.21 Ma for the Pan de Azúcar monzogranite (OD033) from the far north of the study area (Fig. 3), interpreted here as the crystallization age. It is broadly consistent with a previously reported SHRIMP zircon U–Pb age of 276.6 ± 3.6 Ma for monzogranite and 269.5 ± 4.0 Ma for leucogranite (Maksaev et al. 2014), although older than the U–Pb zircon age of 230 ± 8 Ma for the monzogranite reported by Berg and Baumann (1985). Intrusive rocks to the south and east of the El Zorro gold district are younger. Two samples collected from the Sierra El Roble Pluton in the far south of the region (Fig. 3) yielded 163.97 ± 1.63 Ma for granodiorite (OD005) and 162.37 ± 1.31 Ma for alkali granite (TRC024296), consistent with that reported by Girardi (2014) in the same pluton. Crystallization ages for two samples of Las Ánimas granodiorite in the northeast of the region range between 159.56 ± 1.44 (OD035) and 157.21 ± 1.21 (OD023), consistent with U–Pb dates reported in the literature by Berg and Breitkreuz (1983) (159.7 ± 1.6 Ma and 160.0 ± 2.0 Ma) and Gelcich (2006) (156.4 ± 0.3 Ma to 161.0 ± 0.2 Ma). Closer to the El Zorro gold district, intrusive ages converge on the Triassic/Jurassic boundary (Fig. 3). Two samples we analyzed from the Flamenco Pluton yielded a crystallization age of 193.56 ± 2.45 Ma for the granodiorite (OD013) and 190.64 ± 1.91 Ma for the granite (OD011), respectively. Our results are similar to the 195 to 190 Ma range collectively reported by Berg and Breitkreuz (1983), Gelcich (2006), Rodríguez et al. (2019) and Jara et al. (2021a).

A small number of inherited U–Pb zircon ages were obtained from the Pan de Azúcar, Relincho, Sierra El Roble, and Las Ánimas plutons (ESM 1 Table A4).

Intrusions from the El Zorro gold district (26°46′S)

We determined twelve new LA-ICP-MS ages for the Relincho Pluton (Figs. 3 and 4; Table 1). These collectively yield a crystallization range from 205.22 ± 1.73 Ma to 194.12 ± 3.10 Ma. Our results are a little older than those published by Jara et al. (2021a) for a quartz-diorite (192.4 ± 0.9 Ma). In detail, for the tonalites that are the main mineralization host, crystallization ages are 205.22 ± 1.73 Ma to 197.40 ± 2.10 (zircon $n = 5$; Figs. 4 and 8a, b) and are congruent with an additional zircon age of 204.97 ± 1.81 Ma (TRC025711) for similar, but unmineralized tonalite ~ 3 km west of the main mineralization (Fig. 3). A similar age range was obtained in one gabbro sample (TRC024290; Fig. 4) yielding a crystallization age of 203.62 ± 15.29 Ma based on a combined analysis of apatite and titanite crystals (Fig. 8c). Concordia ages for the main granodiorites which cut the El Zorro Tonalites at Ternera yielded an age range between 201.60 ± 2.10 to 199.33 ± 1.61 Ma (Figs. 4 and 8d). However, a slightly later stage of tonalites, dated at 197.40 ± 2.10 Ma (HC01; Fig. 8b), cut these granodiorites 3 km to the west (see below), and at least some of the granodiorite was co-emplaced with tonalite at the southern end of Ternera (Fig. 4).

An age of 194.12 ± 3.10 Ma was obtained for a weakly mineralized lamprophyre dike (HC03; Fig. 8e) that cuts both the 197.40 ± 2.10 Ma tonalite and the 201.60 ± 2.10 Ma granodiorite (Fig. 4). The uncertainty associated with this age is 2–3% due to the limited number of zircon concentrates

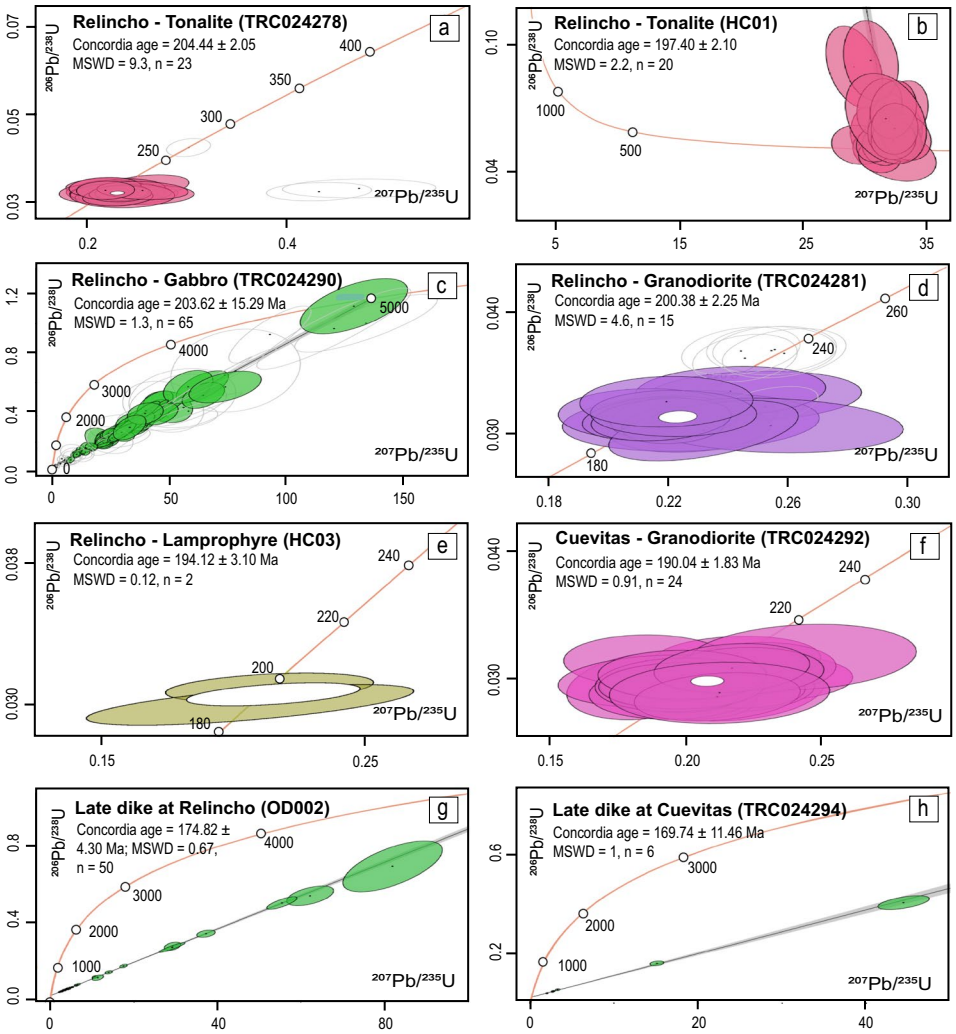

Fig. 8 Wetherill Concordia plots of U–Pb dating results of samples related to the El Zorro gold district. The data for these plots, as well as additional samples, are documented in the ESM 1 Table A4

in the sample, however, field relationships show it is younger than the 197.40 Ma tonalite.

Additionally, two U–Pb ages were obtained for granodiorite samples collected from the Cuevitas Pluton (Fig. 4) and constrain its crystallization age to between 190.74 ± 1.81 (TRC024293) and 190.04 ± 1.83 (TRC024292; Fig. 8f) (Table 1). These results are significantly older than the 159 ± 4 Ma (K–Ar Bt) previously published by Godoy and Lara (1999).

Late dikes

Three samples of the fresh, olivine-bearing basaltic- to andesitic dikes intruding the Flamenco, Relincho and Cuevitas plutons were also analyzed (Figs. 3 and 4). These dikes yielded no zircons, but crystallization ages of U–Pb of apatite obtained were 164.70 ± 9.11 (OD018), 174.82 ± 4.30 (OD002; Fig. 8g) and 169.75 ± 11.46 (TRC024294; Fig. 8h) (Table 1). These values are similar to ^{40}Ar-^{39}Ar whole-rock ages previously published by Dallmeyer et al. (1996) in the region. Importantly, these dikes cut mineralization at Buzzard and Ternera prospects (see below).

Whole-rock geochemical results

The geochemical data for El Zorro gold district provide potential information on the tectonic setting and evolution of the magmatism, the metal fertility, and a wide range of comparisons to other mineralization styles, both globally and within Chile. Given the scope of this paper, here we specifically focus on those aspects of the geochemistry that indicate or distinguish the mineralization style.

Our analyses that include REEs (ESM 1 Table A3) were used to compare with igneous rocks hosting IRG deposits globally, and also with porphyry and IOCG-related intrusive rocks in the Coastal Cordillera in the region around the El Zorro gold district. Spider-grams normalized to N-MORB (Sun and McDonough 1989) show that the trends for El Zorro Relincho and Cuevitas intrusives are very consistent with IRG intrusive rocks presented by Mair

et al. (2011) for the Tintina Gold Province (Yukon, Canada) and to those of Linares (Cepedal et al. 2013) that have previously been inferred to be classic examples of IRGs. There are differences between all three suites regarding W and Mo, reflecting subtle differences in mineralization style, and/or inclusion of some mineralized samples in the data (see Discussion and Conclusions section). Comparing the IRG data (at El Zorro and globally) with the Coastal Cordillera IOCG and porphyry intrusions, the most striking differences between these suites are the clear enrichment in K and the pronounced depletion in P and Ti in the unaltered El Zorro intrusions (Fig. 9). This indicates a higher retention of Ti in insoluble Fe-Ti oxides and distinguishes these rocks from IOCG- and porphyry-related intrusions (Richards et al. 2017 and references therein).

We applied Principal Component Analysis (PCA) to most metals (Ag, As, Au, Bi, Cu, Fe, Mn, Mo, Pb, Sb, Sn, Te, W and Zn) from our larger four-acid digest ICP-MS results from the Ternera deposit and surrounding areas, to assess the metal associations (ESM 1 Table A5). We excluded Se, Ta and Tl due to the high percentage of results below detection limits (but their inclusion or exclusion does not significantly impact the other results). Results are shown in Fig. 10a, in which a distinctive correlation of Au with W and Bi is observed, and somewhat weaker correlation with As, Te and Sn. A weak correlation with Mo is apparent, but there is no obvious relationship to Cu-Pb–Zn, or Fe–Mn, which is also indicated in the full PCA outputs and related correlation matrix (ESM 1 Table A6).

Thompson et al. (1999) and Baker et al. (2005) demonstrated the distinctive nature of IRG-related magmatic rocks and mineralization by determining their approximate redox state relative to total Fe content and compared their results to magmatic rocks from porphyry and other environments. They noted that IRG-related intrusions were characteristically reduced, metaluminous to weakly peraluminous, with distinctive associations of Au with Bi, W and to some extent with Sb, As and locally Mo, and low levels of combined

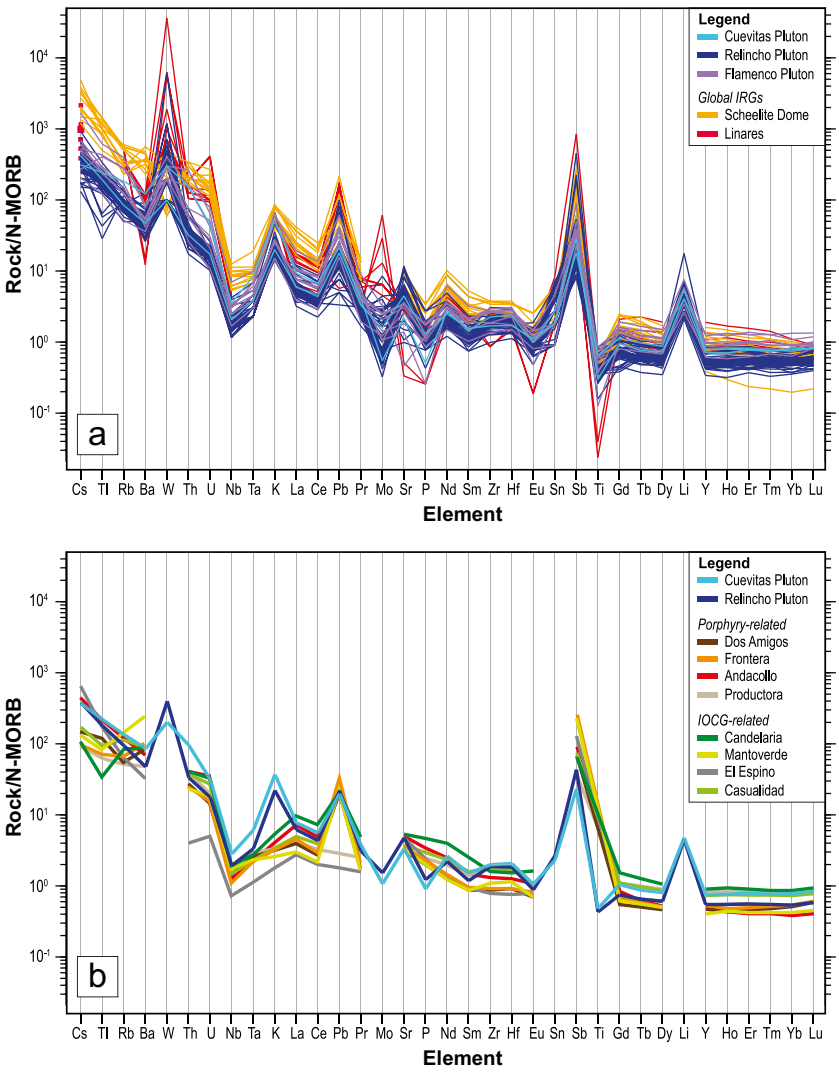

Fig. 9 N-MORB normalized extended trace element diagrams (normalized to values of Sun and McDonough 1989) for least altered igneous rocks. (**a**) Triassic/Jurassic boundary intrusions from the El Zorro district and surrounding areas, compared with global IRG-related intrusions compiled from Mair et al. (2011) and Cepedal et al. (2013). Differences between the districts are largely restricted to W and Mo, which vary within sub-systems of IRG deposits (Robert et al. 2007). (**b**) Averages of El Zorro district intrusions alongside available data from IOCG- and porphyry-related intrusions in the Coastal Cordillera from Richards et al. (2017). Despite the missing elements from Richards et al. (2017) there are substantial differences for many elements and pattern changes for clusters of elements, between the three broad groups

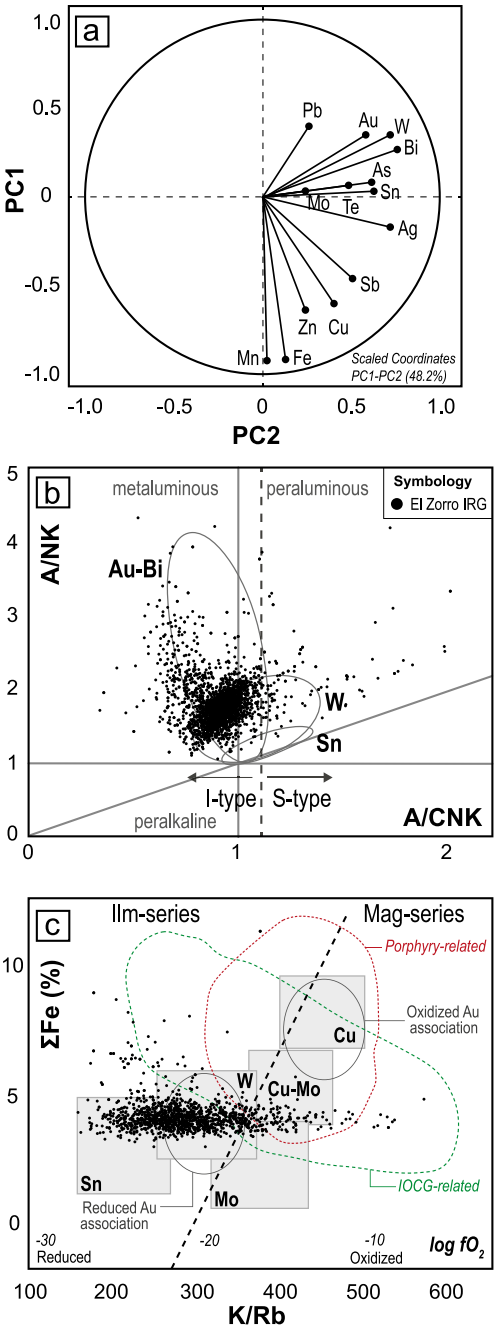

Fig. 10 Data from four-acid digest ICP-MS whole-rock geochemistry results for rocks within and immediately around the Ternera deposit, predominantly analyzed from typical 0.5 to 2 m drill core intervals (ESM 1 Table A5). (**a**) Principal component analysis using ioGAS™ with a classical PCA and log transform of the elements shown, for all rocks within Ternera, showing a strong Au-W-Bi association. PCA results and correlation matrix are in ESM 1 Table A6. (**b**) Data from mineralized to unmineralized tonalite and granodiorite plotted on the Shand's peraluminosity index (Maniar and Piccoli 1989) used for the discrimination between I-type and S-type granitoid rocks, including the IRG metal associations proposed by Baker et al. (2005). (**c**) Data from fresh and weakly altered Ternera tonalite and granodiorite, plotted on this schematic diagram showing magma-metal-redox associations adapted from Thompson et al. (1999). K/Rb ratios (plotted here) are based on its use as a redox proxy for the magnetite-ilmenite series proposed by Blevin (2004), as indicated by the fO_2 axis, but the relationships schematic, because all the Ternera rocks are ilmenite-bearing and magnetite absent. The red and green dashed lines encompass the compositions of little to moderately altered rocks from nearby Coastal Cordillera IOCG-related intrusions and porphyry intrusions presented by Richards et al. (2017). Although they are mostly magnetite-bearing, their position on this diagram reflects uncertainty in the application of the K/Rb proxy to magmatic oxidation state (see text for discussion), but the fields are distinctly different from our Ternera data. Data from mineralized or altered rocks were omitted from this plot if they showed Au > 0.2 ppm, S > 0.7%, strong logged alteration, or K/Na ratios outside the 90-percentile cluster of the median of unaltered rocks (using ioGAS™)

Cu-Pb–Zn. Blevin (2004) also recognized that K/Rb ratios in weakly altered intrusive rocks can act as an imprecise proxy for redox state of those magmas, and noted that most magnetite- and hematite-bearing primary intrusive rocks hosting Cu-Mo ± Au (Pb–Zn) mineralization tend to have higher K/Rb values than reduced, ilmenite-series intrusions with Au-Bi-W ± As-Sb-Sn-Mo.

Figure 10b shows our data for both fresh and mineralized tonalite and granodiorite from Ternera superimposed on the Shand index plot (after Maniar and Piccoli 1989) for the discrimination between I-type and S-type granitoid rocks. Baker et al. (2005) also used this plot to demonstrate the nature and metal associations of IRG intrusive rocks. The Ternera data overlap prominently with the Au-Bi and W fields, consistent with the metal association demonstrated by PCA (Fig. 10a). Figure 10c is a modification of the original schematic diagram of magmatic fO_2 versus total Fe content of Thompson et al. (1999). We have used the K/Rb ratios as a rough proxy for fO_2 of the magma, as discussed by Blevin (2004). Using our four-acid ICP-MS data (ESM 1 Table A5) for fresh to weakly altered and mineralized tonalite and granodiorite from Ternera, our data plot mostly within the W-associated ilmenite-series intrusive field (reiterating that all of these rocks contain ilmenite as a primary accessory mineral). Published geochemistry of least altered porphyry and IOCG-related intrusions from the Coastal Cordillera (Richards et al. 2017) are plotted as broad fields, and these overlap the fields for Cu-Mo and Cu-associated oxidized magmas defined by Thompson et al. (1999). Spread of data outside the defined boxes of Thompson et al. (1999) relates to uncertainties in the connection between K/Rb ratios and the oxidation state of the primary magmas, and potentially some effect of alteration that preferentially affects this ratio, even though we have filtered out the most obviously altered and mineralized data from this particular plot.

Discussion

Temporal and genetic relationships between magmatism and mineralization

New U–Pb ages from this research indicate that the Relincho Pluton crystallized from ~ 205 to 197 Ma, around 80 m.y. younger than the inferred age of regional metamorphism and ductile deformation of the host phyllites (Bahlburg and Hervé 1997). Tonalite dikes from the Relincho Pluton are the main host rocks for the Au-rich Ternera-style deposits and prospects, hence providing a maximum Upper Triassic age for the gold mineralizing event (Fig. 2). Some tonalite dikes (~ 197 Ma) also cut some granodiorite (~ 201 to 199 Ma), and these two rocks appear locally mingled and mixed along some contacts (Fig. 6). The emplacement of the Cuevitas Pluton occurred around ~ 190 Ma. Some mineralized veins and faults cut both the granodiorite of the Relincho and Cuevitas plutons (Fig. 11). Barren olivine-bearing mafic dikes documented at the regional and district scale have U–Pb ages of ~ 175 to 170 Ma, indicating a magmatic event that post-dates the emplacement of the Relincho and Cuevitas plutons (Figs. 4 and 11). This suite of dikes clearly cuts mineralization at Buzzard and Ternera North providing an absolute youngest Middle Jurassic age for mineralization (Fig. 11).

Our U–Pb zircon, monazite, and apatite-titanite results define a clear crystallization age range (205 to 190 Ma) for these Upper Triassic to Lower Jurassic intrusions. Previously published $^{40}Ar/^{39}Ar$ and K–Ar ages for biotite, amphibole and whole-rock and Rb–Sr isochron ages for the Relincho Pluton lie in the range 195 to 180 Ma, and these ages, compared with our U–Pb zircon, monazite, and apatite-titanite ages are consistent with some combination of (a) the lower blocking temperatures for the Rb–Sr, K–Ar and Ar–Ar systems, (b) likely protracted crystallization and cooling history of large plutons in the region, (c) the possibility of influence of slightly younger (Cuevitas) intrusions causing some re-setting of Ar or Rb systems, and (d) the possibility of

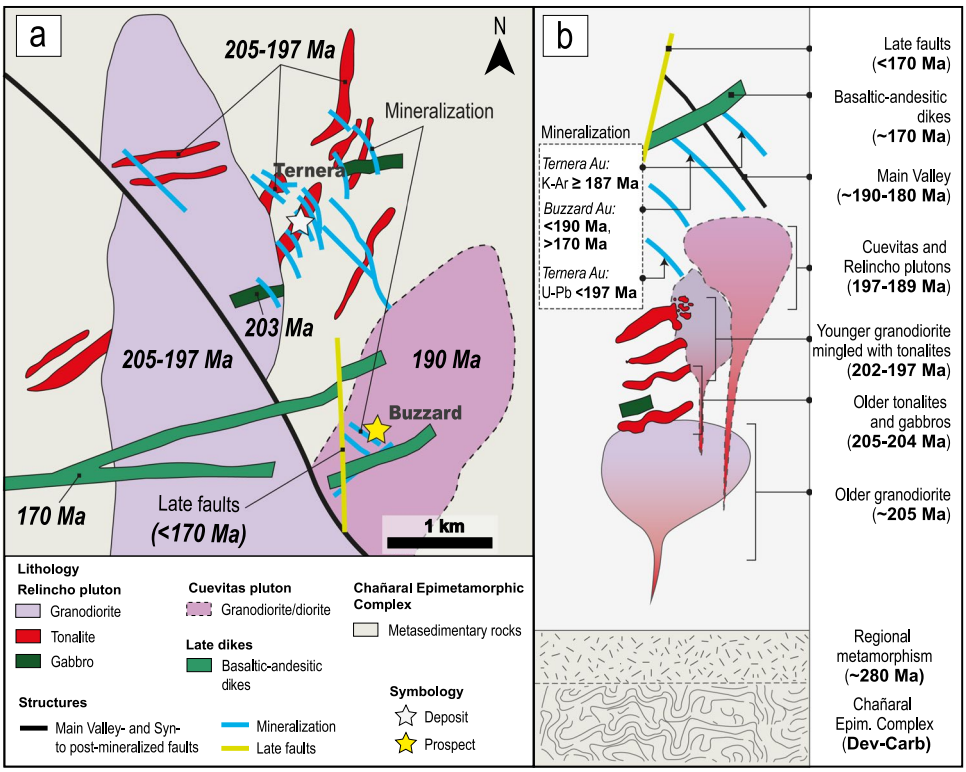

Fig. 11 Map-scale cross-cutting and timing relationships in the El Zorro gold district with corresponding geochronological summary. (**a**) Semi-schematic map with major units simplified (but roughly to scale). Mineralization at Ternera is shown in more detail in Fig. 6. (**b**) Temporal relationships with vertical axis (time). Key geochronological constraints are indicated. Late faults cut all features but the Main Valley- and Syn- to post-mineralization faults (black), and similar smaller ones are cut by 170 Ma mafic dikes (medium green) which in turn cut mineralized faults and major veins (sky blue). Mineralized veins are clustered around and cut the tonalites (red) but are also found in the major intrusions and cutting the older metasedimentary rocks. Lamprophyre dikes (not shown) are commonly found adjacent to or within mineralized structures and are themselves locally strongly mineralized. The mineralization is constrained broadly in the 205 to 170 Ma interval but is most likely to have developed mostly around 190 Ma or progressed from 200 to 185 Ma

hydrothermal events resetting or causing somewhat younger Ar–Ar or K–Ar ages.

An age of 187.0 ± 6.0 Ma (K–Ar on sericitized whole-rock) has been published for Au-related alteration at the Coquetas/Ternera deposit (Vivallo et al. 2008). Together with the zircon and hornblende ages from the adjacent cooling intrusions, these data imply that the mineralization is temporally linked to the emplacement of either Relincho Pluton, which lies at the centre of the currently defined Tenera resource, and/or to the Cuevitas Pluton to the south, which also hosts mineralization (Buzzard prospect, Fig. 4). Along with the relatively large error in the whole-rock K–Ar method, the apparent difference between emplacement of intrusions and the generation of related mineralization is similar to differences reported for many porphyry or IRG systems elsewhere (Hart 2007; Chiaradia and Caricchi 2017; Yu et al. 2022).

Magma compositions and tectonic implications

The geochemistry, the predominance of ilmenite as the main Fe-(Ti) accessory mineral (even partly preserved after alteration to titanite in high-grade ore samples), and the abundance of biotite and hornblende, indicates that primary magmas were hydrous, reduced, ilmenite-series mostly metaluminous calc-alkaline rocks, similar to equivalent rocks in Japan where ilmenite and magnetite-series granitoids were first distinguished (Ishihara 1977). The igneous geochemistry is also very similar to post-collisional intrusions hosting IRG deposits in the Tintina Belt and other IRG belts globally (Mair et al. 2011; Cepedal et al. 2013; Palacios et al. 2014).

Several studies (Ishihara 1977; 2004; Sato 2012) have indicated that the formation of ilmenite-series granitoids in accretionary terranes may be promoted by (1) the mingling of deep mafic magmas with felsic magmas derived from a reduced crust, and (2) the interaction of magma with a carbon-bearing crust during its ascent, which leads to the reduction of the magma. On a regional scale, Jara et al. (2021b) demonstrated a low redox state in magmas of comparable age to those from El Zorro, attributed to the reduced influence of slab fluids during the emplacement of plutons in an attenuated margin soon after the inception of the magmatic arc. We infer that the El Zorro intrusions were generated in this manner.

Despite their proximity to the well-known Cretaceous to Miocene IOCG and porphyry belts of the Coastal Cordillera and pre-frontal Andes, these intrusive rocks and related mineralization are older, and display a different metal association. There is an association of Au with W and Bi, and also with As, Te, and Sn, which are consistent with the associations demonstrated for other IRGs globally (e.g., Baker et al. 2005; Hart 2007; Robert et al. 2007). Notably, gold is not associated with major iron enrichment, copper or other base metals, even though two major IOCG districts lie within tens of km (Fig. 3). Further description and interpretation of the tectono-magmatic connection of this mineralization and its relationship to the adjacent metallogenic belts is outside the scope of this paper and will be presented later.

Gold mineralization commonly occurs in sheeted arrays of parallel, low sulfide (~0.1 to 2%), quartz ± calcite veins and veinlets, with the most abundant sulfides being pyrite, pyrrhotite and arsenopyrite. Alteration is most commonly spatially restricted to narrow (mm- to dm-scale) vein selvages, and albite, biotite and K-feldspar 'bleaching' dominate the alteration around the moderately to strongly mineralized samples. Much mineralization is specifically hosted by the intrusions but extends out into the country rocks also. These features are very similar to characteristics of the Tintina Belt 'type localities' for IRGs.

Most importantly, and the major focus of this paper, is that the timing of mineralization is bracketed by and related to the emplacement of a distinct suite of intrusions with IRG characteristics. The direct genetic association of mineralization with a causative magma is a distinguishing feature of many IRGs (Hart 2007; An et al. 2022; Yu et al. 2022). We also observed magmatic-hydrothermal transition textures (Fig. 7h, i) also observed at other IRG deposits (Cepedal et al. 2013).

Conclusions

The El Zorro gold district represents the oldest and westernmost mineralizing event in northern Chile. Field cross-cutting relationships, along with newly obtained geochronological results, demonstrate that gold mineralization is Upper Triassic to Lower Jurassic, most likely in the range 200 to 185 Ma, the oldest ages yet assigned to Au mineralization in Chile (Fig. 2). These findings are consistent with its time–space placement within the tectonic framework of easterly-younging mineralization and igneous activity in the Chilean Cordillera.

We strongly support the classification of the El Zorro gold district as the first defined IRG system of the Chilean Coastal Cordillera. This is evidenced by the cutting of earlier orogenic fabrics, the metal and alteration associations, and the spatial and temporal connection to reduced ilmenite-series intrusions, which exhibit geochemical similarities to the 'type-locality' IRG intrusions of the Tintina Belt in Yukon/Alaska.

IRG and orogenic gold deposits represent underexplored and under-investigated targets in the Coastal Cordillera. We suggest there are several other potential zones of Triassic/Jurassic IRGs in western Chile, either identified previously as "mesothermal gold" or not yet discovered.

Supplementary Information The online version contains supplementary material available at https://doi.org/10.1007/s00126-024-01324-w.

Acknowledgements Tesoro Gold Ltd is thanked and acknowledged for funding and field support for the project. Thanks to all the El Zorro gold project staff for their support during and after fieldwork, and special thanks to Rubén Cahuana for his help in the field and excellent geological discussions. Eduardo Fritis is grateful for a grant from the Faculty of Science, University of Auckland that funded this work, and also acknowledges the Faculty of Science at the University of Auckland for providing access to the Microscopy Laboratory facilities. A special thanks goes to Andres Arcila-Rivera and David Adams for their technical support. Mike Cooley is recognized for his contribution in generating some of the structural and mapping data. Aaron Tomsett from Cube Consulting is thanked for his support with the database transfers. Avish Kumar is acknowledged for his help with mineral separation, CL imaging and data acquisition. The authors also would like to thank Darren Richardson from Ingham Petrographics for the preparation of thin sections. We thank Tim Baker, an anonymous reviewer, and assistant editor Fernando Tornos for their review and editorial comments, Karen Kelley for her overall editorial input, and John Thompson for discussions.

Authors' contribution Eduardo Fritis: Field work, data processing and interpretation, figure drawing, main writer of the manuscript.

Nicholas H. S. Oliver: Field work, data processing and interpretation, figure drawing, manuscript reviewer, writer of the manuscript, supervision.

Michael C. Rowe: Field work, data processing, manuscript reviewer, supervision.

Julie V. Rowland: Field work, manuscript reviewer, financial support, supervision.

Zeffron C. Reeves: Field work, financial support.

Huiqing Huang: Data processing and interpretation.

Funding Open Access funding enabled and organized by CAUL and its Member Institutions.

Declarations

Competing interests The authors declare the following financial interests/personal relationships which may be considered as potential competing interests: Eduardo Fritis reports financial support was provided by Faculty of Science, University of Auckland. Eduardo Fritis reports financial support was provided by Tesoro Gold Ltd.

References

Aliyari F, Rastad E, Mohajjel M (2012) Gold deposits in the sanandaj–sirjan zone: orogenic gold deposits or intrusion-related gold systems? Resour Geol 62:296–315. https://doi.org/10.1111/j.1751-3928.2012.00196.x

ALS (2022) Schedule of Services & Fees. ALS Global. https://www.alsglobal.com/. Accessed 15 Feb 2022

An F, Zhu Y, Lehmann B, Zheng B, Qiang J (2022) The Baogutu gold deposit in west Junggar, NW China: an epizonal intrusion-related gold deposit. Ore Geol Rev 150:105188. https://doi.org/10.1016/j.oregeorev.2022.105188

Bahlburg H, Hervé F (1997) Geodynamic evolution and tectonostratigraphic terranes of northwestern Argentina and northern Chile. Geol Soc Am Bull 109:869–884. https://doi.org/10.1130/0016-7606(1997)109%3c0869:GEATTO%3e2.3.CO;2

Bahlburg H, Vervoort JD, DuFrane SA, Bock B, Augustsson C (2009) Timing of accretion and crustal recycling at accretionary orogens: insights learned from the western margin of South America. Earth Sci Rev 97:227–253. https://doi.org/10.1016/j.earscirev.2009.10.006

Baker T, Pollard PJ, Mustard R, Mark G, Graham JL (2005) A comparison of granite-related tin, tungsten, and gold-bismuth deposits: implications for exploration. SEG Discovery 61:5–17. https://doi.org/10.5382/SEGnews.2005-61.fea

Barra F, Reich M, Selby D, Rojas P, Simon A, Salazar E, Palma G (2017) Unraveling the origin of the Andean IOCG clan: A Re-Os isotope approach. Ore Geol Rev 81:62–78. https://doi.org/10.1016/j.oregeorev.2016.10.016

Behn G, Camus F, Carrasco P, Ware H (2001) Aeromagnetic signature of porphyry copper systems in northern Chile and its geologic implications. Econ Geol 96:239–248. https://doi.org/10.2113/gsecongeo.96.2.239

Berg K, Baumann A (1985) Plutonic and metasedimentary rocks from the Coastal Range of northern Chile: Rb-Sr and U-Pb isotopic systematics. Earth Planet Sci Lett 75:101–115. https://doi.org/10.1016/0012-821X(85)90093-7

Berg K, Breitkreuz C (1983) Mesozoische Plutone in der Nordchilenischen Kustenkordillere: Petrouenese. Geochronologie, Geochemie und Geodynamik mantelbetonter magmatique. Geotek Forsch 66:1–107

Bierlein FP, Groves DI, Cawood PA (2009) Metallogeny of accretionary orogens—the connection between lithospheric processes and metal endowment. Ore Geol Rev 36:282–292. https://doi.org/10.1016/j.oregeorev.2009.04.002

Blevin PL (2004) Redox and compositional parameters for interpreting the granitoid metallogeny of eastern Australia: implications for gold-rich ore systems. Resour Geol 54:241–252. https://doi.org/10.1111/j.1751-3928.2004.tb00205.x

Brook M, Pankhurst RJ, Shepherd TJ, Spiro B, Snelling N, Swainbank I (1986) Andchron: Andean geochronology and metallogenesis. Overseas Development Administration, London

Cabello J (2021) Gold Deposits in Chile. Andean Geol 48:1–23. https://doi.org/10.5027/andgeoV48n1-3294

Cahill T (1990) Earthquakes and tectonics of the central Andean subduction zone. PhD Dissertation, Cornell University

Camus F, Dilles JH (2001) A special issue devoted to porphyry copper deposits of northern Chile. Econ Geol 96:233–237. https://doi.org/10.2113/gsecongeo.96.2.233

Cepedal A, Fuertes-Fuente M, Martín-Izard A, García-Nieto J, Boiron MC (2013) An intrusion-related gold deposit (IRGD) in the NW of Spain, the Linares deposit: Igneous rocks, veins and related alterations, ore features and fluids involved. J Geochem Explor 124:101–126. https://doi.org/10.1016/j.gexplo.2012.08.010

Charrier R, Pinto L, Rodríguez MP (2007) Tectonostratigraphic evolution of the Andean Orogen in Chile. In: Moreno T, Gibbons W (eds) The Geology of Chile. The Geol Soc, London, pp 21–114. https://doi.org/10.1144/GOCH

Chen H, Cooke DR, Baker MJ (2013) Mesozoic iron oxide copper-gold mineralization in the Central Andes and the Gondwana supercontinent breakup. Econ Geol 108:37–44. https://doi.org/10.2113/econgeo.108.1.37

Chiaradia M, Caricchi L (2017) Stochastic modelling of deep magmatic controls on porphyry copper deposit endowment. Sci Rep 7:44523. https://doi.org/10.1038/srep44523

Creixell C, Oliveros V, Vásquez P, Navarro J, Vallejos D, Valin X, Godoy E, Ducea MN (2016) Geodynamics of Late Carboniferous-Early Permian forearc in north Chile (28°30′–29°30′S). J Geol Soc 173:757–772. https://doi.org/10.1144/jgs2016-010

Dallmeyer RD, Brown M, Grocott J, Taylor GK, Treloar PJ (1996) Mesozoic magmatic and tectonic events within the Andean plate boundary zone, 26–27 30'S, North Chile: constraints from $^{40}Ar/^{39}Ar$ mineral ages. J Geol 104:19–40. https://doi.org/10.1086/629799

del Real I, Reich M, Simon AC, Deditius A, Barra F, Rodríguez-Mustafa M, Thompson JFH, Roberts MP (2023) Formation of giant iron oxide-copper-gold deposits by superimposed episodic hydrothermal pulses. Sci Rep 13:12041. https://doi.org/10.1038/s41598-023-37713-w

Escolme A, Cooke DR, Hunt J, Berry RF, Maas R, Creaser RA (2020) The Productora Cu-Au-Mo Deposit, Chile: A Mesozoic magmatic-hydrothermal breccia complex with both porphyry and iron oxide Cu-Au affinities. Econ Geol 115:543–580. https://doi.org/10.5382/econgeo.4718

Firth EA, Holwell DA, Oliver NH, Mortensen JK, Rovardi MP, Boyce AJ (2015) Constraints on the development of orogenic style gold mineralisation at Mineral de Talca, Coastal Range, central Chile: evidence from a combined structural, mineralogical, S and Pb isotope and geochronological study. Miner Deposita 50:675–696. https://doi.org/10.1007/s00126-014-0568-6

Fuentes P, Díaz-Alvarado J, Rodríguez N, Fernández C, Breitkreuz C, Contreras AA (2018) Geochemistry, petrogenesis and tectonic significance of the volcanic rocks of the Las Tortolas Formation, Coastal Cordillera, northern Chile. J South Am Earth Sci 87:66–86. https://doi.org/10.1016/j.jsames.2017.11.006

García M, Maksaev V, Townley B, Dilles J (2017) Metallogeny, structural evolution, post-mineral cover distribution and exploration in concealed areas of the northern Chilean Andes. Ore Geol Rev 86:652–672. https://doi.org/10.1016/j.oregeorev.2017.01.025

Gelcich SH (2006) Early Andean subduction-related magmatism, northern Chile (-26.5˚S); Geochronology (e.g. U-Pb), isotopic geochemistry (Hf) and Fe-oxide Cu Au mineralization. PhD Thesis, University of Toronto

Girardi JD (2014) Comparison of Mesozoic magmatic evolution and iron oxide (-copper-gold) ('IOCG') mineralization, Central Andes and western North America. PhD Thesis, The University of Arizona

Godoy E, Lara L (1998) Hojas Chañaral y Diego de Almagro. Región de Atacama, Servicio Nacional de Geología y Minería, Santiago

Godoy E, Lara L (1999) Hoja Puerto Flamenco. Región de Atacama, Servicio Nacional de Geología y Minería, Santiago

Godoy E, Marquardt C, Blanco N (2003) Carta Caldera. Región de Atacama, Servicio Nacional de Geología y Minería, Santiago

Gow PA, Walshe JL (2005) The role of preexisting geologic architecture in the formation of giant porphyry-related Cu±Au deposits: Examples from New Guinea and Chile. Econ Geol 100:819–833. https://doi.org/10.2113/gsecongeo.100.5.819

Grocott J, Taylor GK (2002) Magmatic arc fault systems, deformation partitioning and emplacement of granitic complexes in the Coastal Cordillera, north Chilean Andes (25°30′ S to 27°00′ S). J Geol Soc 159:425–443. https://doi.org/10.1144/0016-764901-124

Groves DI, Santosh M, Deng J, Wang Q, Yang L, Zhang L (2019) A holistic model for the origin of orogenic gold deposits and its implications for exploration. Miner Deposita 55:275–292. https://doi.org/10.1007/s00126-019-00877-5

Hart CJR (2007) Reduced intrusion-related gold systems. In: Goodfellow WD (ed) Mineral deposits of Canada: a synthesis of major deposit types, district metallogeny, the evolution of geological provinces, and exploration methods. Geological Association of Canada, Mineral Deposits Division, Special Publication No. 5, pp 95–112

Hart CJR, Goldfarb RJ (2005) Distinguishing intrusion-related from orogenic gold systems. Proceedings of the New Zealand Minerals Conference, Auckland, New Zealand, pp 125–133

Hervé F, Faundez V, Calderón M, Massonne H-J, Willner AP (2007) Metamorphic and plutonic basement complexes. In: Moreno T, Gibbons W (eds) The Geology of Chile. The Geol Soc, London, pp 201–214. https://doi.org/10.1144/GOCH.2

Hervé F, Calderón M, Fanning CM, Pankhurst RJ, Navarro J (2020) U-Pb SHRIMP detrital zircon dating of metamorphic rocks in north–central Chile (28°–33° S): Evidence for Carboniferous and Triassic metamorphism in a subduction setting. J South Am Earth Sci 103:102767. https://doi.org/10.1016/j.jsames.2020.102767

Ishihara S (1977) The magnetite series and ilmenites series granitic rocks. Min Geol 27:293–305. https://doi.org/10.11456/shigenchishitsu1951.27.293

Ishihara S (2004) The redox state of granitoids relative to tectonic setting and earth history: the magnetite–ilmenite series 30 years later. Trans R Soc Edinb Earth Sci 95:23–33. https://doi.org/10.1017/s0263593300000894

Jara JJ, Barra F, Reich M, Morata D, Leisen M, Romero R (2021a) Geochronology and petrogenesis of intrusive rocks in the Coastal Cordillera of northern Chile: Insights from zircon U-Pb dating and trace element geochemistry. Gondwana Res 93:48–72. https://doi.org/10.1016/j.gr.2021.01.007

Jara JJ, Barra F, Reich M, Leisen M, Romero R, Morata D (2021b) Episodic construction of the early Andean Cordillera unravelled by zircon petrochronology. Nat Commun 12:4930. https://doi.org/10.1038/s41467-021-25232-z

Kojima S, Soto I, Quiroz M, Valencia P, Fernandez I (2017) Geological and Geochemical Characteristics of the Intrusion-Related Vein-Type Gold Deposits in the El Morado District, Coastal Cordillera, Northern Chile. Resour Geol 67:197–206. https://doi.org/10.1111/rge.12129

Lang JR, Baker T (2001) Intrusion-related gold systems: the present level of understanding. Miner Deposita 36:477–489. https://doi.org/10.1007/s001260100184

Lara L, Godoy E (1998) Hoja Quebrada Salitrosa, Región de Atacama. Servicio Nacional de Geología y Minería, Santiago

Lucassen F, Franz G (1996) Magmatic arc metamorphism: petrology and temperature history of metabasic rocks in the Coastal Cordillera of northern Chile. J Metamorph Geol 14:249–265. https://doi.org/10.1046/j.1525-1314.1996.59011.x

Mair JL, Farmer GL, Groves DI, Hart CJ, Goldfarb RJ (2011) Petrogenesis of postcollisional magmatism at Scheelite Dome, Yukon, Canada: evidence for a lithospheric mantle source for magmas associated with intrusion-related gold systems. Econ Geol 106:451–480. https://doi.org/10.2113/econgeo.106.3.451

Maksaev V, Munizaga F, Fanning M, Palacios C, Tapia J (2006) SHRIMP U-Pb dating of the Antucoya porphyry copper deposit: new evidence for an Early Cretaceous porphyry-related metallogenic epoch in the Coastal Cordillera of northern Chile. Miner Deposita 41:637–644. https://doi.org/10.1007/s00126-006-0091-5

Maksaev V, Townley B, Palacios C, Camus F (2007) Metallic ore deposits. In: Moreno T, Gibbons W (eds) The Geology of Chile. The Geol Soc, London, pp 179–199. https://doi.org/10.1144/GOCH.6

Maksaev V, Munizaga F, Tassinari C (2014) Temporalidad del magmatismo del borde paleo-Pacífico de Gondwana: geocronología U-Pb de rocas ígneas del Paleozoico tardío a Mesozoico temprano de los Andes del norte de Chile entre los 20 y 31 S. Andean Geol 41:447–506. https://doi.org/10.5027/andgeoV41n3-a01

Maniar PD, Piccoli PM (1989) Tectonic discrimination of granitoids. GSA. Bulletin 101:635–643. https://doi.org/10.1130/0016-7606(1989)101%3c0635:TDOG%3e2.3.CO;2

Maureira I, Barra F, Palma G (2022) Geology of the Altamira and Las Luces deposits, Coastal Cordillera, northern Chile: implications for the origin of stratabound Cu–(Ag) deposits. Miner Deposita 58:379–402. https://doi.org/10.1007/s00126-022-01132-0

Oliveros V, Féraud G, Aguirre L, Fornari M, Morata D (2006) The Early Andean Magmatic Province (EAMP): $^{40}Ar/^{39}Ar$ dating on Mesozoic volcanic and plutonic rocks from the Coastal Cordillera, northern Chile. J Volcanol Geotherm Res 157:311–330. https://doi.org/10.1016/j.jvolgeores.2006.04.007

Oliveros V, Vásquez P, Creixell C, Lucassen F, Ducea MN, Ciocca I, González J, Espinoza M, Salazar E, Coloma F, Kasemann SA (2020) Lithospheric evolution of the Pre- and Early Andean convergent margin, Chile. Gondwana Res 80:202–227. https://doi.org/10.1016/j.gr.2019.11.002

Orlandea E, Vlad SN (2020) A novel conceptual model of intrusion-related gold- bearing systems and exploration tools. Studia UBB Geol 63:1–12. https://doi.org/10.5038/1937-8602.63.1.1304

Oyarzún J (2000) Andean metallogenesis: a synoptical review and interpretation. In: Cordani UG, Milani EJ, Thomaz Filho A, Campos DA (eds) Tectonic evolution of South America. 31st International Congress, Rio de Janeiro, pp 725–753

Palacios S, Alfonso P, Proenza JA (2014) Mineralogy and geochemistry of the IRG Misky gold deposit, southern Peru. EGU General Assembly, Viena, pp 15618

Reinoso F, Marquardt M, Cembrano J, Pérez-Flores P, Díaz-Alvarado J, Folguera A (2024) Tectonic setting, structures, and Au–Cu mineralization age of the Indiana deposit: An example of ore deposit formation controlled by Andean transverse faults, Atacama region. Chile. J South Am Earth Sci 133:104705. https://doi.org/10.1016/j.jsames.2023.104705

Reyes M (1991) The Andacollo strata-bound gold deposit, Chile, and its position in a porphyry copper-gold system. Econ Geol 86:1301–1316. https://doi.org/10.2113/gsecongeo.86.6.1301

Richards JP, Mumin AH (2013) Magmatic-hydrothermal processes within an evolving Earth: Iron oxide-copper-gold and porphyry Cu±Mo±Au deposits. Geology 41:767–770. https://doi.org/10.1130/G34275.1

Richards JP, López GP, Zhu JJ, Creaser RA, Locock AJ, Mumin AH (2017) Contrasting tectonic settings and sulfur contents of magmas associated with Cretaceous porphyry Cu±Mo±Au and intrusion-related iron oxide Cu-Au deposits in northern Chile. Econ Geol 112:295–318. https://doi.org/10.2113/econgeo.112.2.295

Robert F, Brommecker R, Bourne BT, Dobak PJ, McEwan CJ, Rowe RR, Zhou X (2007) Models and exploration methods for major gold deposit types. In: Milkereit B (ed) Proceeding of Exploration 07: Fifth Decennial International Conference on Mineral Exploration, Toronto, Canada, 9–12 September 2007, pp 691–711

Rodríguez N, Díaz-Alvarado J, Fernández C, Fuentes P, Breitkreuz C, Tassinari CCG (2019) The significance of U-Pb zircon ages in zoned plutons: the case of the Flamenco pluton, Coastal Range batholith, northern Chile. Geosci Front 10:1073–1099. https://doi.org/10.1016/j.gsf.2018.06.003

Rodríguez N, Díaz-Alvarado J, Fernández C, Breitkreuz C, Fuentes P, Merida G (2021) Relation between intrusive and deformational processes in oblique subductive margins. The case of the zoned Flamenco pluton in northern Chile. J South Am Earth Sci 112:103553. https://doi.org/10.1016/j.jsames.2021.103553

Sato K (2012) Sedimentary Crust and Metallogeny of Granitoid Affinity: Implications from the Geotectonic Histories of the Circum-Japan Sea Region, Central Andes and Southeastern Australia. Resour Geol 62:329–351. https://doi.org/10.1111/j.1751-3928.2012.00200.x

SERNAGEOMIN (2003) Mapa Geológico de Chile: versión digital. Servicio Nacional de Geología y Minería, Publicación Geológica Digital, No. 4 (CD-ROM, versión 1.0, 2003). http://www.ipgp.fr/~dechabal/Geol-millon.pdf. Accessed 10 Nov 2021

Seymour NM, Singleton JS, Mavor SP, Gomila R, Stockli DF, Heuser G, Arancibia G (2020) The Relationship Between Magmatism and Deformation Along the Intra-arc Strike-Slip Atacama Fault System, Northern Chile. Tectonics 39:1–29. https://doi.org/10.1029/2019TC005702

Sillitoe RH (1972) Relation of Metal Provinces in Western America to Subduction of Oceanic Lithosphere. Geol Soc Am Bull 83:813–818. https://doi.org/10.1130/0016-7606(1972)83[813:ROMPIW]2.0.CO;2

Sillitoe RH (2003) Iron oxide-copper-gold deposits: an Andean view. Miner Deposita 38:787–812. https://doi.org/10.1007/s00126-003-0379-7

Sun SS, McDonough WF (1989) Chemical and isotopic systematics of oceanic basalts: implications for mantle composition and processes. Geol Soc Spec Publ 42:313–345. https://doi.org/10.1144/GSL.SP.1989.042.01.19

Takagi T, Tsukimura K (1997) Genesis of oxidized-and reduced-type granites. Econ Geol 92:81–86. https://doi.org/10.2113/gsecongeo.92.1.81

Thompson JFH, Sillitoe RH, Baker T, Lang JR, Mortensen JK (1999) Intrusion-related gold deposits associated with tungsten-tin provinces. Miner Deposita 34:323–334. https://doi.org/10.1007/s001260050207

Tornos F, Hanchar JM, Munizaga R, Velasco F, Galindo C (2021) The role of the subducting slab and melt crystallization in the formation of magnetite-(apatite) systems, Coastal Cordillera of Chile. Miner Deposita 56:253–278. https://doi.org/10.1007/s00126-020-00959-9

Vivallo W, Díaz A, Jorquera R (2008) Yacimientos metalíferos de la Región de Atacama. Servicio Nacional de Geología y Minería, Santiago

Whitney DL, Evans BW (2010) Abbreviations for names of rock-forming minerals. Am Mineral 95:185–187. https://doi.org/10.2138/am.2010.3371

Yu HC, Qiu KF, Sai SX, McIntire DC, Pirajno F, Duo DW, Miggins DP, Wang J, Jia RY, Wu MQ (2020) Paleo-tethys late triassic orogenic gold mineralization recorded by the Yidi'nan gold deposit, West Qinling. China Ore Geol Rev 116:103211. https://doi.org/10.1016/j.oregeorev.2019.103211

Yu L, Sun F, Beier C, Wu D, Li L, Wang L, Huang G, Fan X, Xu C (2022) Geology, U-Pb geochronology and stable isotope geochemistry of the Heihaibei gold deposit in the southern part of the Eastern Kunlun Orogenic Belt, China: A granitic intrusion-related gold deposit? Ore Geol Rev 144:104859. https://doi.org/10.1016/j.oregeorev.2022.104859